**ORIGINAL RESEARCH PAPER**

# Depositional influence of submarine channel migration on thermal properties of the Lower Fangliao Basin, offshore southwestern Taiwan

Feisal Dirgantara[1,2] · Hsieh-Tang Chiang[3] · Andrew Tien-Shun Lin[1,2] · Char-Shine Liu[4] · Song-Chuen Chen[5]

## Abstract

The depositional history of the paleo-submarine channel plays an instrumental role in controlling the present-day heat flows and geothermal gradients of the Lower Fangliao Basin, a slope basin situated at the upper accretionary wedge, offshore southwestern Taiwan. This wedge is formed from the collision of the Luzon Arc and the Chinese continental margin. The basin has been referred as one of the gas-hydrate prospective areas within the vicinity, where occurrence of mud diapirs and bottom-simulating reflectors (BSRs) is present. Estimated BSRs-derived geothermal gradients infer an average value of 33 °C km$^{-1}$, while estimated heat flows imply an average value of 41 mW m$^{-2}$. Closely spaced thermal probes and infrared imaging from piston cores revealed average values for geothermal gradients and heat flows of 55 °C km$^{-1}$ and 62 mW m$^{-2}$, respectively. Discrepancies between both measurements are related to the sensitivity of direct thermal measurements over shallow fluid flux, where shallow geothermal gradients increase locally as the fluid migrates upward. Since the BSRs are situated at depths below cut-and-fill channel deposits in the basin depocenter, the channel facies is interpreted as deposition of an active channel prior to being intruded by mud diapirs and abandoned in the Pleistocene. An array of data, including high-resolution seafloor bathymetry, seismic facies, and distribution of thermal anomaly, reveal that the paleo-channel had flowed through the Lower Fangliao Basin following the strike of slope basins and deposited a stacked series of turbidite sands. Submarine ridges in the upper slope of the accretionary wedge developed as thrust-related anticlines, which bordered the slope basins. Rapid deposition and sediment burial in offshore southwestern Taiwan had caused insufficient dewatering process in the paleo-channel sediments, leaving high water saturation within pore spaces and overpressured the sediments. These, together, lead to lower heat flows and thermal gradients (thermal blanketing effect) and contribute to deepen the base of gas hydrate stability zone. Further mud diapiric intrusions and uplifting of seafloors had blocked the course of paleo-channel. The Lower Fangliao Basin was abandoned following the channel course shifted to the south along the present-day Gaoping Canyon course.

✉ Andrew Tien-Shun Lin
andrewl@ncu.edu.tw

1    Taiwan International Graduate Program – Earth System Science Program, Academia Sinica, Taipei 11529, Taiwan

2    Department of Earth Sciences, National Central University, No. 300, Zhongda Rd., Zhongli District, Taoyuan 32001, Taiwan

3    Center for General Education, National Ilan University, No. 1, Sec. 1, Shennong Rd., Yilan City 260, Yilan County, Taiwan

4    Ocean Center, National Taiwan University, No. 1, Sec. 4, Roosevelt Rd., Taipei 10617, Taiwan

5    Central Geological Survey, Ministry of Economic Affairs, No. 2, Ln. 109, Huaxin St., Zhonghe Dist, New Taipei City 235, Taiwan

## Introduction

Heat flow estimation in the offshore region of an orogenic wedge possesses vital information to the thermal signature and how it evolves during the formation of accretionary wedge. However, evaluation of thermal properties of an orogenic belt is challenging as the crustal deformation and associated thermal evolution are time-dependent (e.g., Song and Ma 2002). As one of the youngest and most active mountain belt on earth, crustal deformation and seismicity of the Taiwan island are still actively on going due to the convergence of the Philippine Sea and the Eurasian Plates. The offshore southwestern Taiwan has undergone major tectonic shift from subduction to collision tectonic episodes, resulting in the development of the foreland basin to the west of the Taiwan orogen (Lin and Watts 2002). In the foreland basin, a linear depression formed from the flexure of foreland lithosphere under the load of the orogenic wedge, the thermal structure is typically cooler than normal lithosphere, where heat flows range between 42 and 84 mW m$^{-2}$ (Allen and Allen 2013). Unlike most convergent zones around the world, where decreasing heat flow trends are present from trenches to shallow shelves (Jessop 1990; Lewis et al. 2003), the heat flow profile in Taiwan increases from subduction zone to collision zone (Chi and Reed 2008). The anomaly can be seen as a combination effect of rapid rock exhumation, increased erosion, and induced groundwater circulation (Chi and Reed 2008). As opposed to regional lithospheric scale effects on basin temperatures, localized thermal events (e.g. magma intrusion, diapirism), internal discrepancies of fluid flow, and isolated thermal conductivity variations could perturb the present-day basin temperatures dramatically (Blackwell and Steele 1989).

The Lower Fangliao Basin is an offshore, semi-enclosed slope basin situated at the upper Taiwan accretionary wedge, where diapiric activities have influenced its morphology (Sun and Liu 1993; Yu and Lu 1995; Yu and Huang 2006; Chen et al. 2014). With widely distributed bottom simulating reflectors (BSRs), the basin has been regarded as one of gas hydrate-bearing provinces in offshore southwestern Taiwan (Hsu et al. 2017; Dirgantara et al. 2020). BSRs have been used to derive heat flow distribution, both in passive continental margins (Li et al. 2013; Liu et al. 2006; Liao et al. 2014) and active continental margin (Kaul et al. 2000; Chi and Reed 2008). Since the formation of gas hydrate stability is more susceptible to changes in temperature than pressure (Shyu et al. 2006), heat flow information, which reflects subsurface temperature variations, plays a paramount constraint to understand the thermal evolution in a sedimentary basin. Previous studies within the vicinity of the Lower Fangliao Basin

inferred average heat flows in the submarine accretionary wedge of Taiwan ranging from 43 mW m$^{-2}$ (Chi and Reed 2008) to 64 mW m$^{-2}$ (Shyu et al. 2006). By knowing the temperature at the seabed, geothermal gradients and heat flows can be estimated from BSRs (e.g. Davis et al. 1990; Shyu et al. 2006; Liu et al. 2006). Alternatively, thermal properties retrieved by piston or gravity cores can be measured directly either in situ on the seafloor or by subsequent assessments on sediments retrieved from the seafloor. In situ thermal measurements can be derived by inverting the decay of calibrated heat signals (Hartmann and Villinger 2002) using heat probes, whereas infrared imaging has been used to identify thermal anomalies on sediment cores (Weinberger et al. 2005; Rothwell and Rack 2006). Thermobaric model of hydrate stability zone can be established when the geothermal gradient intersects the hydrate phase boundary, or known as base of gas hydrate stability (BGHS). While direct relationship between BSRs and BGHS is absent, BSRs can be treated as approximation to BGHS due to prominent temperature influence on gas hydrate stability and assuming negligible effect of salinity, pressure, and encapsulated hydrocarbon gas composition (Mandal et al. 2014). Therefore, seismically defined BSRs can be used to provide additional constraints on the thermal properties at continental margins in a wider scale, where direct thermal measurement is hindered by penetration depths.

General consensus regarding sedimentation and tectonic activities towards the thermal characters in offshore southwestern Taiwan have been proposed by previous studies (Shyu et al. 1998, 2006; Chi et al. 1998; Chi and Reed 2008). However, none of these studies discuss the relationship between thermal properties on their relationship with the depositional environment on basin scale. This study intends to investigate heat flow and geothermal gradient anomalies in the Lower Fangliao Basin based on BSRs-derived estimation, in situ measurement using heat probes and thermal infrared imaging of sediment cores; and how the thermal complexion link to the evolution of the Lower Fangliao Basin. Three dimensional seismic data is utilized to define the spatial BSRs distribution. BSRs-derived heat flow estimations serve to complement heat flow measurements carried out in the upper accretionary slope region by previous studies (Chi et al. 1998; Shyu et al. 1998, 2006; Liu et al. 2006; Chi and Reed 2008). Direct heat flow measurements from heat probe and infrared thermal imaging within the basin depocenter are used to constraint the BSRs-estimated heat flow values. Corrections for measured heat flows and geothermal gradients are calculated using two scenarios of sedimentation rates. BGHS, which marks the base of hydrate boundary under specific geothermal gradient, is derived to constrain the BSRs depths. Interpretation of 2D seismic data are

incorporated to delineate the potential paleo-canyon continuity in the northern part of the study area. Both thermal history and seismic interpretation efforts are combined to build the history of the Lower Fangliao Basin.

## Regional geology

The area off southwestern Taiwan has experienced collisional-to-subduction transition of the frontal zone from
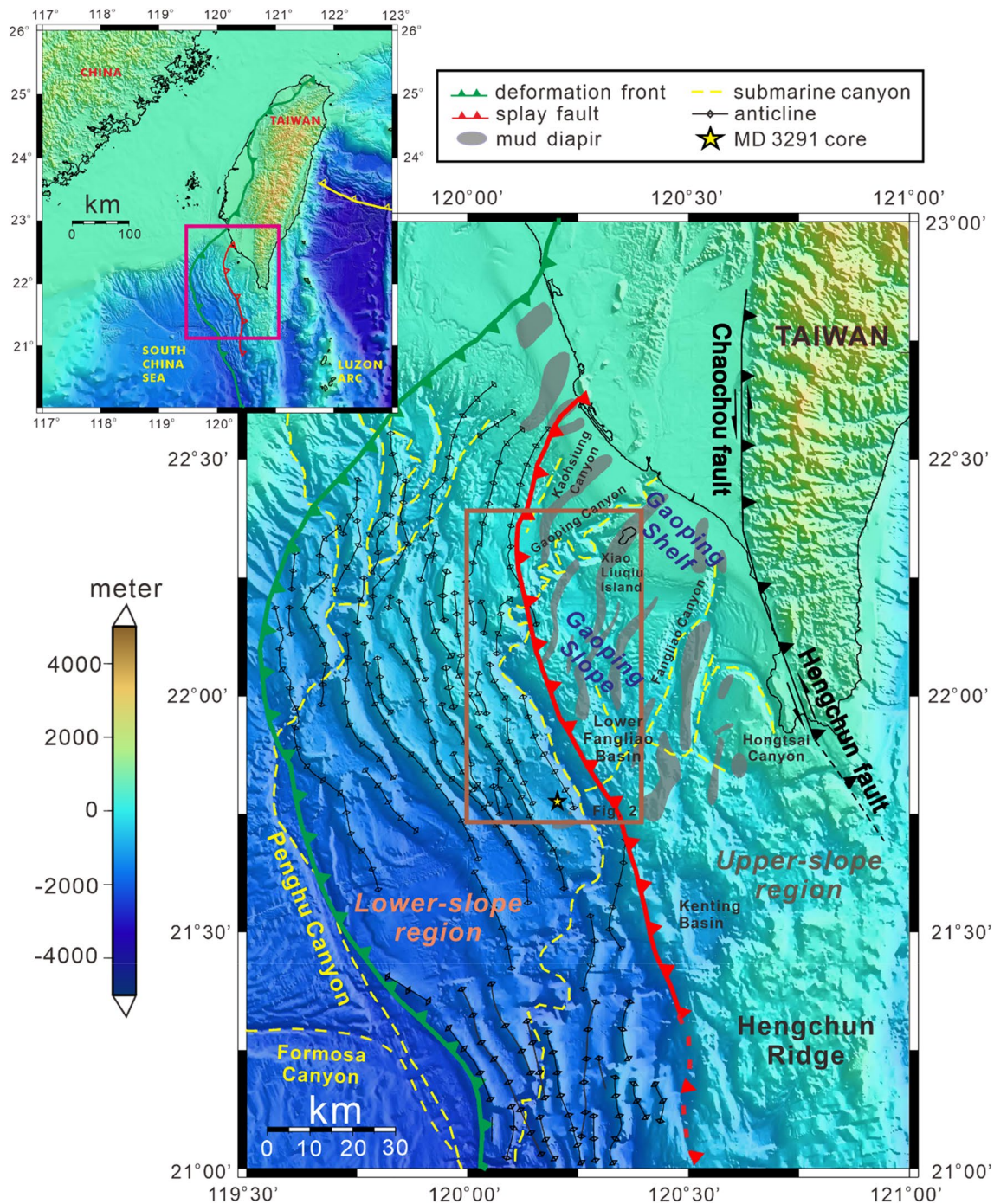


**Fig. 1** Tectonic elements in the Taiwan region with inset showing regional geology features. The offshore zone southwest of Taiwan is an area where Luzon subduction system encroaches on China continental margin, transforming the subduction system into an incipient arc-continent collision complex. Brown square shows the vicinity of study area in Fig. 2. The offshore structures are modified from Lin et al. (2008, 2009a)

initial oblique collision between Luzon Arc of the Philippine Sea Plate and the Eurasian Plate along the passive margin of southeast China since the late Miocene (Lin and Watts 2002) (Fig. 1). The area is also where the outgrowth of submarine accretionary wedge extends westward to the Chinese continental margin and prominent morphological features developed, e.g. submarine canyons and anticlinal ridges (Lin et al. 2008). Reed et al. (1992) subdivided the western incipient collisional wedge into the lower slope domain and upper slope domain. Both domains are dominated by off-scraped continental margin strata and orogenic sediments derived from the Taiwan mountain belts. A deformation front bounds the western limit of the lower slope domain with the continental margin. The upper slope domain is characterized by localized active deformation, a series of mud diapirs, and weak seismic reflections. The latter could be associated with steeply dipping beds within the upper slope vicinity (Sun and Liu 1993; Chi et al. 1998). The boundary between the lower slope and the upper slope marks the out-of-sequence thrusting within the wedge (Lin et al. 2009a). Presence of mud volcanoes in both onshore and offshore of the collisional wedge infers intense fluid expulsion within the accretionary wedge (Yang et al. 2004; Chiu et al. 2006).

In offshore southwestern Taiwan, basin formation pertaining to mud diapirism has been subjected to debate in the past two decades. Sun and Liu (1993) considered unbalanced loading by thick sediments in paleo-submarine canyons and channels in the upper accretionary wedge as a main factor to localize high pressure of fluid, which later stimulates the hitherto mud-cored anticlines formed during subsequent arc-continent collision into present-day mud diapirism. On the other hand, Yu and Lu (1995) suggested pre-collision thick mudstones as protolith for mud diapirs prior to the migration of overpressured mudstones following the north-south trending deformation from the later formation of progressive mud diapir series. Due to distinct positive gravity anomalies than their surroundings, Doo et al. (2015) advocated tectonic compression as primary control for the formation of mud diapirs, instead of buoyancy from the underlying sediments. Alternatively, development of mud diapirism has been ascribed as combined factors of overpressured sediments, compressional forces from the collision, and migration of gas-bearing fluids from deeper strata (Lacombe et al. 2004; Chen et al. 2014).

Morphologically, the offshore area of southwestern Taiwan can be subdivided into the Gaoping Shelf and the Gaoping Slope (Fig. 1). As one of slope basins in the Gaoping Slope, the Lower Fangliao Basin has emerged by mud diapirism since 1.8 Ma in the lower part of the Fangliao Canyon (Hsu et al. 2013) (Fig. 2). At the outer shelf, the canyon head exhibits V-shaped geometry and evolves to a wide U-shaped cross section, before deepening and broadening in the down canyon direction (Yu and Wen 1991). While connectivity

to river mouth on land is limited, sediment transport processes within the basin include mass movements, submarine canyon feeding, and over-spilling processes (Yu and Huang 2006; Hsu et al. 2017). Although BSRs-based heat flows inferred increasing trend from the frontal wedge towards the inner Taiwan mountain belts with values ranging from 15 to 146 mW m$^{-2}$ (Chi and Reed 2008), thermal-probe measurements suggested anomalously high heat flows, up to 170 mW m$^{-2}$, to occur near the summit of mud diapirs in the Gaoping Slope (Shyu et al. 1998). Despite the absence of direct thermal measurement in the Lower Fangliao Basin, heat flows in the northern limit of the basin range from 50 (Shyu et al. 1998) to 73 mW m$^{-2}$ (Shyu et al. 2006).
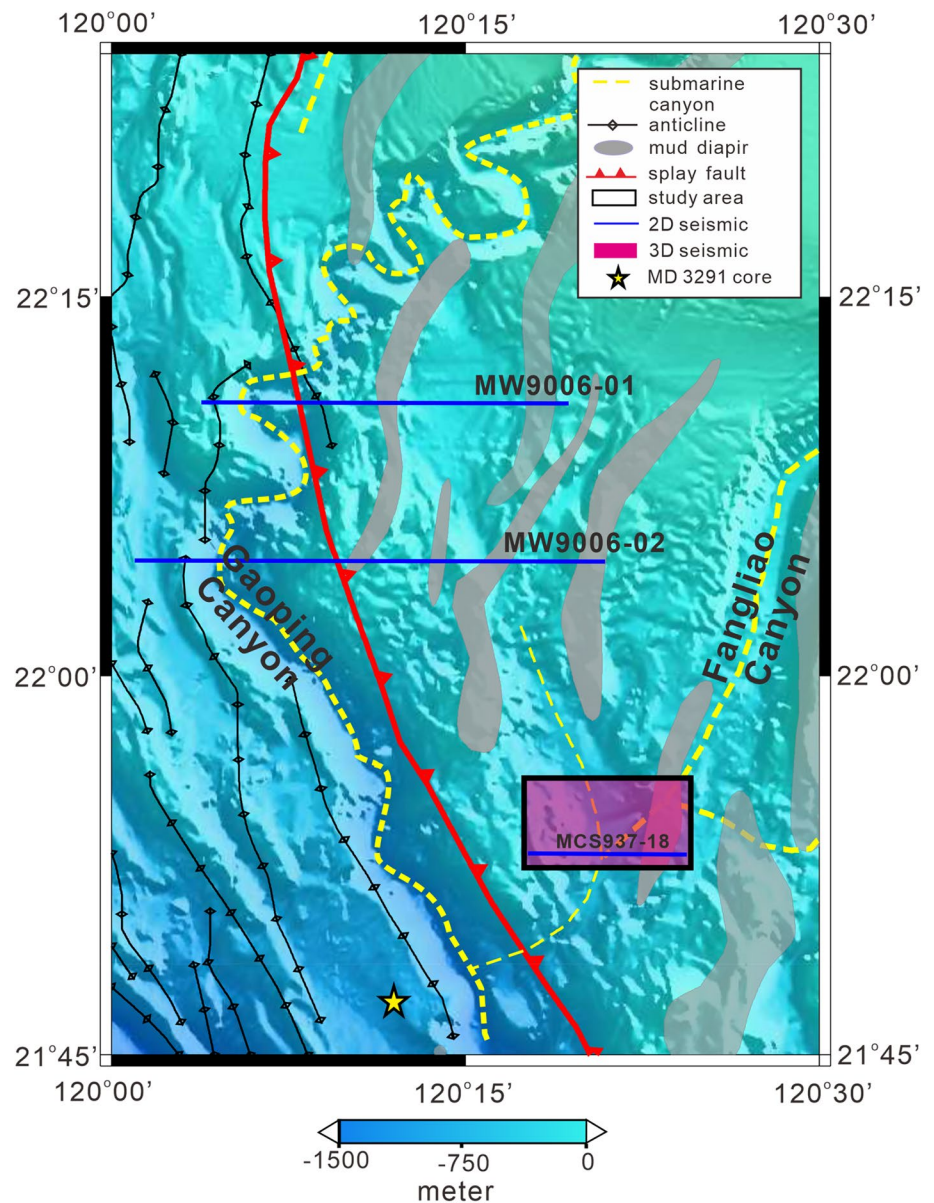
## Methodology

### Seismic data and analyses

Two marine seismic data sets collected onboard *R/V Ocean Researcher I* (OR1) were employed in this study (Fig. 2). The pseudo 3-D seismic data (MCS937) collected in 2010 was achieved using 84 channels, 1 ms sampling rate, 12.5 m channel spacing, 6 m cable depth, 104 inlines, 1000 crosslines, and 50 m of inline spacing. An air-gun array with capacity ranged up to 275 in$^3$ in total volume was fired in every 10 s interval and towed at a depth of 5 m. These dense seismic lines cover a total line length of more than 1000 km and an area of 60 km$^2$. Seismic data processing was performed in the Institute of Oceanography, National Taiwan University. Processing sequence includes trace editing, geometry setup, band-pass filter, amplitude compensation, predictive deconvolution, spiking noise removal, velocity analysis, normal moveout correction, stacking, water velocity F–K time migration, and water column mute. Details regarding the processing workflow have been discussed in Hsu et al. (2017). The same dataset has been employed by Dirgantara et al. (2020) to elucidate the gas-hydrate potential in the Lower Fangliao Basin. A 2D seismic profile, MCS937-18, was extracted from the MCS937 3D seismic volume (Fig. 2).

The second data set was collected in 1990 by *R/V Moana Wave* scientific cruise of the University of Hawaii. The 2-D seismic data (MW9006-01 and MW9006-02) were achieved under 6 channel seismic survey with a 2 airgun (460 in$^3$) array at an average line of 8 km. Data processing was done at UC Santa Cruz and San Jose State University using SIOSEIS processing package. The processing sequence was as follows (Reed et al. 1992): debias correction, decimation of 4 ms, spectral analysis, trace editing, geometry definition, automatic gain control (AGC), spiking deconvolution, NMO correction, stack (four fold), band-pass filter, predictive deconvolution, water-bottom mute, trace weighting, band-pass

**Fig. 2** Reflection seismic line distribution and bathymetry within the vicinity of the Lower Fangliao Basin. Seismic data used in this research are MCS937 3D seismic volume (shown as pink-shaded rectangular box) and the 2D seismic profiles: MCS937-18, MW0906-01, and MW0906-02 (depicted by blue lines)



filter, AGC, stack section, water velocity F–K migration, band-pass filter, AGC, and migrated plot section. The same dataset has been utilized by previous authors for tectonics studies (Reed et al. 1992; Fuh et al. 1994; Lundberg et al. 1997), morphology of submarine canyon study (Liu et al. 1993), and gas hydrates distribution study (Chi et al. 1998) in the offshore southwestern Taiwan. The total length of original seismic lines is 136 and 141 km for MW9006-01 and MW9006-02, respectively, extending from the lower accretionary wedge to the upper accretionary wedge in an E–W direction. However, for the purpose of this study, the main focus for both lines is highlighted only to the area in the upper accretionary wedge (Fig. 2).

The 3D MCS937 seismic volume was used to derive heat flow estimation based on BSRs depth within the target area.

The area occupies the eastern side of the Gaoping Canyon in the upper Gaoping Slope where widespread BSRs are discernible (Chi et al. 1998; Liu et al. 2006). Three seismic profiles (MCS937-18, MW9006-01, and MW9006-02) were interpreted to characterize the subsurface geological condition with regards to the development of paleo-submarine canyon. Seismic surveys in both data sets were designed to achieve parallel lines crossing the structural trend in the upper slope region.

## Thermal properties derived from BSRs depth

Geothermal heat is transferred and distributed through crust by conduction, convection, and/or advection (Turcotte and Schubert 1982). Local conductive heat flow can be estimated

from the depths of BSRs (Kaul et al. 2000; Liu et al. 2006; Li et al. 2013; Liao et al. 2014) by assuming linear temperature gradient and purely conductive heat transfer. Under the assumption that the gas composition and seawater salinity are constant and pore pressure is normal, the BSRs depth is mainly controlled by the geothermal gradient (He et al. 2014). The heat flow is calculated according to 1-D Fourier's law as follows:

$$Q = -K \frac{dT}{dy} = -K \frac{T_{BSR} - T_{sf}}{Z_{BSR}} \qquad (1)$$

where $Q$ is heat flow (mW m$^{-2}$); $K$ is thermal conductivity (W m$^{-1}$ K$^{-1}$); is geothermal gradient (°C km$^{-1}$); $T_{BSR}$ is temperature at BSR depth (°C); $T_{sf}$ is the temperature at seafloor (°C); $Z_{BSR}$ is the depth of BSRs in meter below seafloor (mbsf). Sub-bottom depth of BSRs can be identified from seismic data and computed using Hamilton's approach (1980):

$$Z_{BSR} = 1511t + 1041t^2 - 372t^3 \qquad (2)$$

where $t$ is one-way travel time below seafloor. This relationship was deemed the best estimation for offshore southwestern Taiwan based on geo-acoustic model in continental terraces for the Pacific region (Hamilton 1980). Assuming BSRs define the phase equilibrium boundary of gas hydrate, heat flow estimation can be derived as a function of BSR sub-bottom depths against the water depth. In convergent margin, the geothermal gradient can be estimated by determining temperatures at seafloor and at BSR. Pressure at BSR sub-bottom depths, $P$, for a given water depth, $y$, is calculated as follows:

$$P = \rho_w g y + \rho g Z_{BSR} + P_0 \qquad (3)$$

where $\rho_w$ is water density (kg m$^{-3}$); $g$ is standard gravity constant (9.8 m s$^{-2}$); is sediment density above BSR (kg m$^{-3}$); $P_o$ is atmospheric pressure (pascal). Since the upper slope of accretionary wedge is dominated by muds, the water density and bulk sediment density near the seafloor were assumed to be 1025 and 1700 kg m$^{-3}$, respectively (Shyu et al. 2006). Temperature of phase equilibrium boundary, $T_{BSR}$, is defined as follows (Gayet et al. 2005; Liu et al. 2006; Liao et al. 2014):

$$\mathrm{Ln}\left(\frac{P}{P_0}\right) = 33.4 - \frac{8245}{T}, 275.15\,\mathrm{K} \leq T \leq 286.15\,\mathrm{K} \qquad (4)$$

$$\mathrm{Ln}\left(\frac{P}{P_0}\right) = 41.636 - \frac{10602}{T}, 286.15\,\mathrm{K} \leq T \leq 300.15\,\mathrm{K} \qquad (5)$$

The calculation of thermal conductivity is referred to an empirical solution by Davis et al. (1990). The approach

was suggested on geometric mean model and a mean grain conductivity of 2.4 W m$^{-1}$ K$^{-1}$, an equitable value for clay mineral rich sediments (Riedel et al. 2006). This assumption satisfies the clay-rich sediments character in the offshore southwestern Taiwan (Jiang et al. 2006). The empirical approach can be defined as follows:

$$K = 1.07 + 5.86 \cdot 10^{-4} \cdot Z_{BSR} - 3.24 \cdot 10^{-7} \cdot Z_{BSR}^2 \qquad (6)$$

Seafloor temperature, $T_{SF}$ (°C), is calculated by least-squares approach from measured water temperature and water depth (m), $D$, in the offshore southwestern Taiwan from database archived in National Center of Ocean Research of Taiwan (Chi and Reed 2008) as follows:
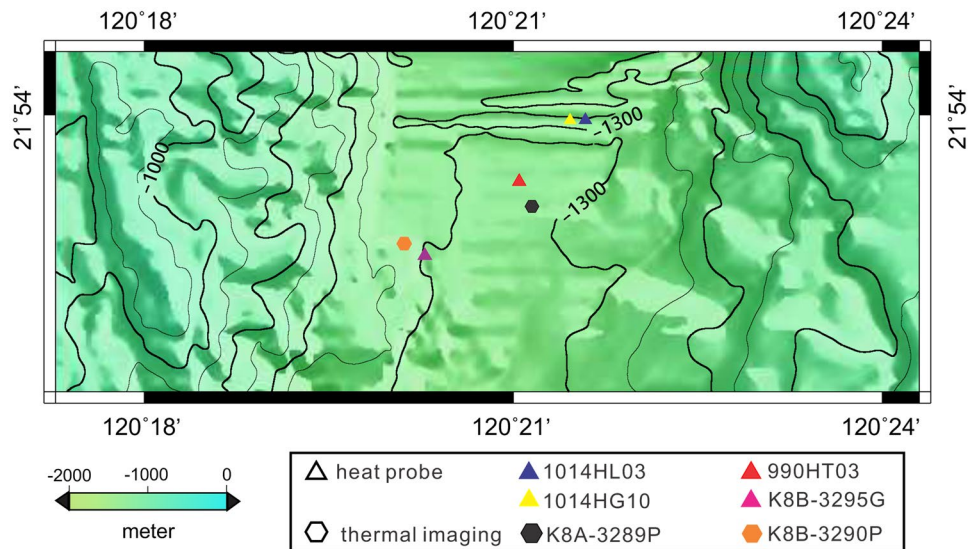
$$T_{SF} = 0.2597 \cdot (\ln D)^3 - 3.802 \cdot (\ln D)^2 + 10.67 \cdot (\ln D) + 26.96 \qquad (7)$$

Geothermal gradients can be derived when BSRs temperature and seafloor temperature are known. Consequently, since geothermal gradients and thermal conductivity are known, heat flow estimation of the study area can be obtained.

## Heat flow measurement from heat probe and infrared camera imaging

Four direct heat flow measurements, namely 990HT03, 1014HG10, 1014HL03, and K8B-3295G, were collected onboard *R/V Marion Dufresne* (MD) in 2010, and R/V OR1 in 2012. These sites are situated in the depocenter of the Lower Fangliao Basin (Fig. 3). Developed by Institute of Oceanography, National Taiwan University, two types of instrument were employed to conduct the measurement. The first type is of the Lister type heat probe with dimension of 7.5 m in length and 800 kg in weight. This probe includes a light temperature sensor tube with dimension of 6.0 m in length and 1.0 cm in diameter (Shyu et al. 1998; Shyu et al. 2006). High temperature resolution is capable of reaching 0.0001 °C sensitivity in the range of − 1 to 25 °C (Shyu and Chang 2005). A heating source was installed within the heat probe, launching the heat automatically for 15 s for 10 min after heat probe penetrates the seafloor. The equilibrium temperature and the thermal conductivity of sediments could be estimated by fitting the temperature decay curve with the thermal decay model of a cylinder (Bullard 1954; Carslaw and Jaeger 1959). At the beginning of measurement, the sensor tube records would increase due to sediment friction when the heat probe penetrated the seafloor. Regression of temperature decay was applied with respect to parameters of ambient temperature, thermal conductivity, initial temperature rise, and heat capacity of the sediment (Shyu and Chang 2005). The second type is the temperature logger with dimension

**Fig. 3** Bathymetry map of the Lower Fangliao Basin based on 3D reflection seismic MCS937 (Dirgantara et al. 2020) with site locations for heat probe and infrared thermal imaging measurements



of 24 cm in length and 2.2 cm in diameter (Chiang et al. 2010). Four temperature loggers were mounted on the wall of a 14 m-long core in every 4 m spacing. This allowed direct thermal gradient measurement when the sediment temperatures were determined. Thermal conductivity was examined by measuring the sediment core on board based on thermal needle probe.

In addition to contact measurements, two sites of infrared camera imaging, namely K8A-3289P and K8B-3290P, were employed to evaluate the thermal gradient of sediment core as a remote detection (Fig. 3). Infrared core scanning was carried out as soon as the sediment core was retrieved from the seawater. Thermal anomaly was identified by marking the indicative tape along the core liner. A thermal camera (FLIR ThermoVision SC4000) was mounted on a cart with a black opaque plastic sheet to maintain the darkness of the space between the camera and the core liner. Thermal images detected by the camera were recorded at a rate of 10 frames/second. The temperatures of core liner were retrieved from the images by using the FLIR ThermaCam Researcher software under a sampling interval of 0.015 m. Thermal gradient calculation from thermal images falls under the assumption that the temperature of the whole sediment core increases consistently during core retrieval process.

## Geothermal gradient corrections

Sedimentation is capable to lower geothermal gradient by blocking the heat transfer from subsurface and perturb the thermal equilibrium. Correction for geothermal gradient is achievable by the following equation (Kappelmeyer and Haenel 1974):

$$G_c = \frac{G}{(1 + \Omega)} \tag{8}$$

where $G_c$ is corrected geothermal gradient (°C km$^{-1}$), $G$ is measured geothermal gradient (°C km$^{-1}$). The correction factor $\Omega$ is given by:

$$\Omega = \frac{1}{2}\left( \frac{v_s^2\tau}{k} - \left(2 + \frac{v_s^2\tau}{k}\right)erf(\frac{v_s\tau}{2\sqrt{k\tau}}) - \left(\frac{2v_s\tau}{\sqrt{\pi k\tau}}\right)exp\left(\frac{-v_s^2\tau}{4k}\right) \right) \tag{9}$$

where is sedimentation rate (mm year$^{-1}$), $\tau$ is duration of sedimentation (year), $k$ is thermal diffusivity (m$^2$ s$^{-1}$), and "$erf$" denotes the error function. Thermal diffusivity defines the ratio of thermal conductivity to heat capacity ($\rho c$) of the sediment. As suggested by previous studies (Hyndman et al. 1979; Shyu et al. 2006), the heat capacity follows:

$$\rho c = (5.79 - 3.67K + 1.016K^2)10^6 \, J \, m^{-3}K^{-1} \tag{10}$$

## Results

### BSRs distribution

A total number of 104 seismic profiles from MCS937 were examined to define the BSRs depth. BSRs are ubiquitous in the study area beneath water depth ranging from 700 to around 1000 m. Structural highs and lows, formed mainly by mud diapirism in the Lower Fangliao Basin, are discernible from the 3D seismic profile (Fig. 4). Dirgantara et al. (2020) defined the study area as a depocenter flanked by mud-diapiric ridges on either side. Striking reflectivity of BSRs can be depicted by the
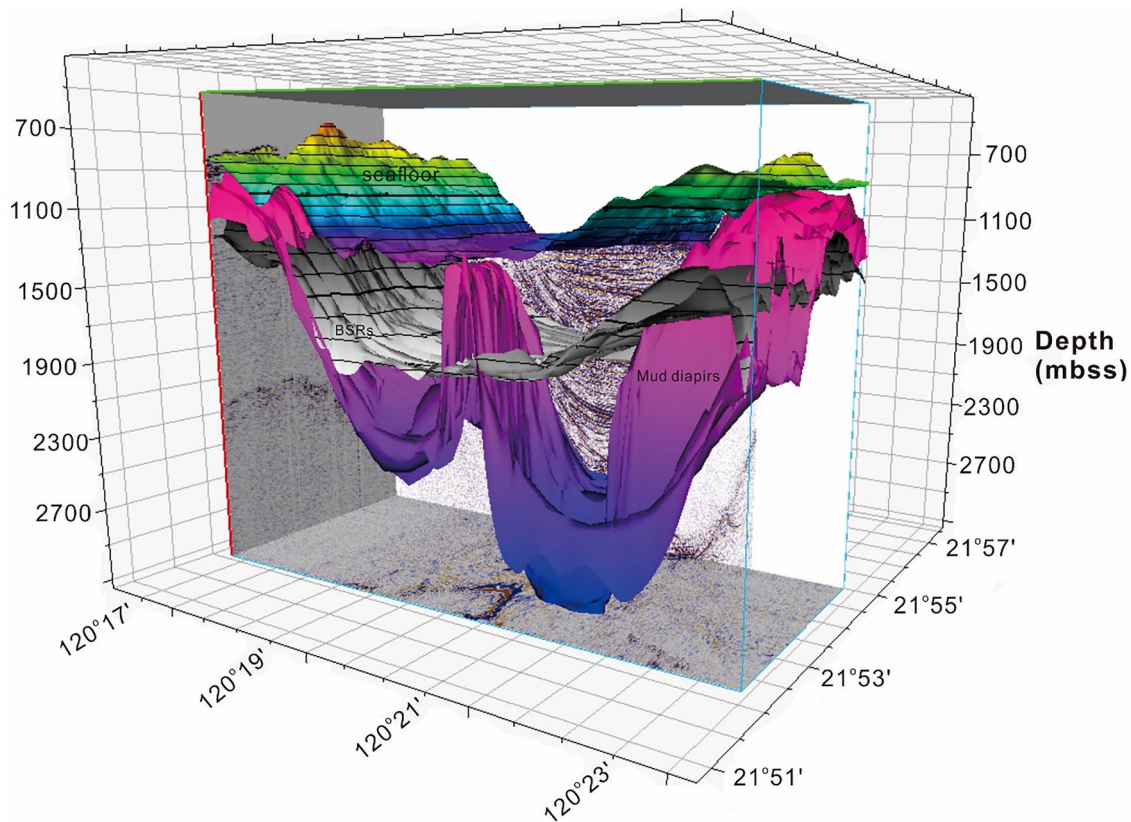
**Fig. 4** 3D configuration of the Lower Fangliao Basin showing seafloor morphology, mud diapirs, and BSRs (Dirgantara et al. 2020). *mbss* meter below sea surface

reversed polarity to that of seafloor, indicating a sudden decrease in acoustic impedance, particularly a sharp drop in P-wave velocity (Zhang and McMechan 2006). These reflections mark phase boundary separating the low-temperature stable phase of solid gas hydrates over a field of free gas instability underneath (Chi et al. 1998). Previous studies suggested extensive accumulation of gas hydrates were present at the passive continental margin and the accretionary wedge offshore southwestern Taiwan, as inferred from the BSRs anomalies at water depth between 100 and 800 m (Reed et al. 1992; Chi et al. 1998; Schnurle et al. 2004; Liu et al. 2006). A broader scale of BSRs distribution covering the entire slope of accretionary wedge aims to shed a qualitative depth comparison of BSRs between the lower slope and the upper slope regions (Fig. 5). The general trend infers shallowing depth of BSRs from the lower slope to the upper slope regions. Anomalously, deeper BSRs are observable in the Lower Fangliao Basin where the depths span from 200 to 550 m beneath the seafloor despite located in the upper slope domain (Fig. 6).

## Heat flow estimation based on BSRs depth

Assuming BSRs define the lower bound of gas hydrate stability zone (GHSZ), gas hydrate stability curves in the offshore southwestern Taiwan can be plotted as a relationship between BSRs sub-bottom depths versus water depth under lithostatic pressure condition (Liu et al. 2006). Under constant temperature assumption of seafloor $T_0 = 3.85$ °C and average thermal conductivity of sediment $K = 1.0$ W m$^{-1}$ K$^{-1}$, a set of methane hydrate stability curves is plotted for heat flow values $Q$ ranging from 20 to 70 mW m$^{-2}$ (Fig. 7). In general, the depth of sub-bottom BSRs shows positive correlation with seafloor depth, except in minor areas where depth variations are present. Derived temperatures of BSRs extend from 14.96 to 20.11 °C with an average temperature of 18 °C. Once the BSRs depths are known, empirical thermal conductivity can be derived, giving range values from 1.14 to 1.33 W m$^{-1}$ K$^{-1}$ with an average value of 1.25 W m$^{-1}$ K$^{-1}$. Assuming the temperature on seafloor-sediment interface is similar to that of the seawater, derived seafloor temperatures range from 3.58 to 5.64 °C with an average
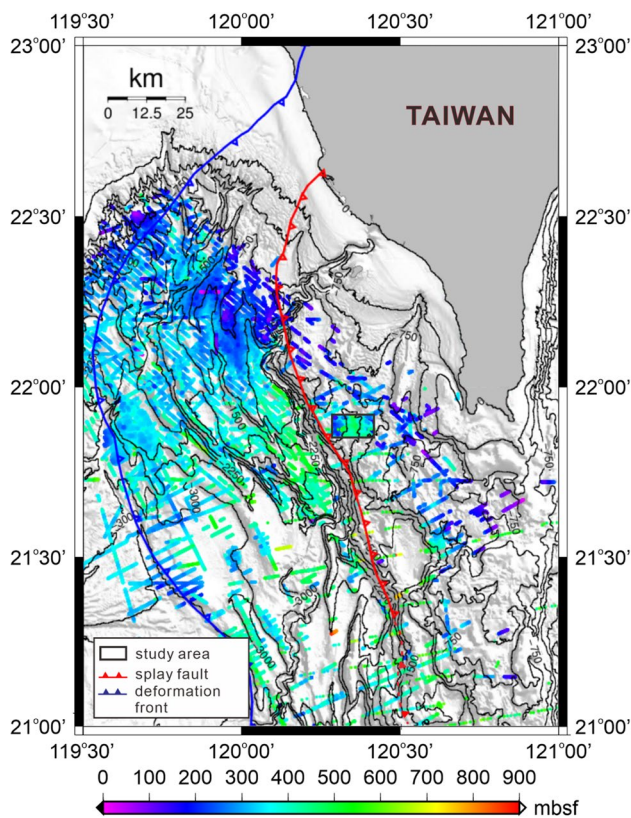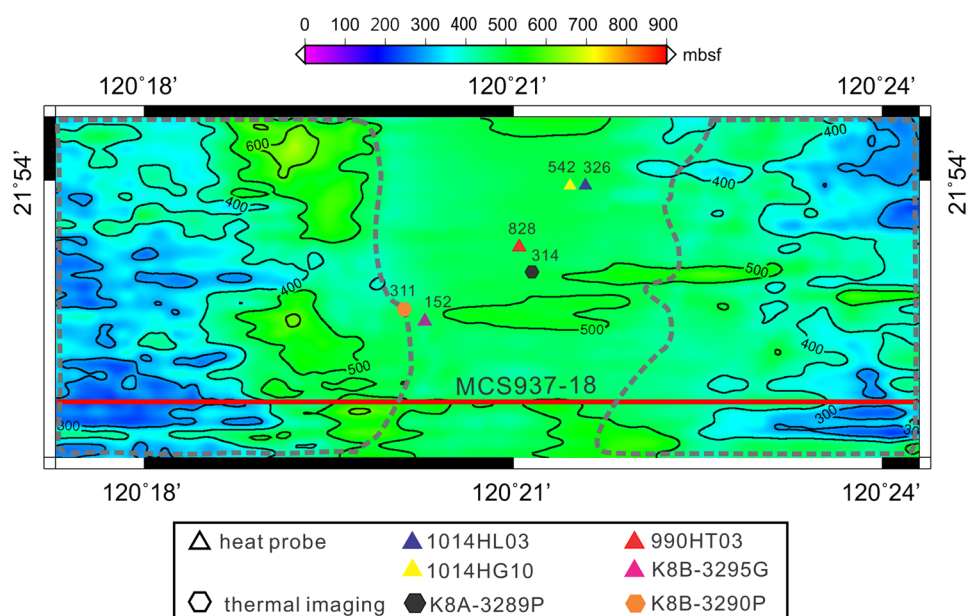
**Fig. 5** Bathymetric map of the study area showing distribution and depths of BSRs in lower slope and upper slope of Taiwan accretionary wedge from Liu et al. (2006) and Chi and Reed (2008). Depths of BSRs are shown in blue to green color with increasing depths. Black square indicates the 3D seismic dataset (MCS937). The BSRs depths are anomalously deeper in the study area compared to other region in the upper slope. *mbsf* meter below seafloor

value of 4.24 °C. Geothermal gradients can then be readily derived once temperatures at both BSRs and seafloor are known, varying from 18.94 to 80.14 °C km$^{-1}$ with an average value of 33 °C km$^{-1}$ (Fig. 8). Since thermal conductivity and geothermal gradients are known, heat flow can be estimated. Under lithostatic condition, the best fit heat flows from BSRs estimation range from 25.24 to 91.55 mW m$^{-2}$ with an average value of 41 mW m$^{-2}$ (Fig. 9) and standard deviation of 4.57. Relatively high heat flow values are discernible in southwestern, southeastern, and northeastern parts of the study area, where mud diapirs are present.

## Heat flow based on contact measurement and infrared camera imaging

With a median value of 55 °C km$^{-1}$, four sites of in situ thermal contact measurements and two sites of infrared camera imaging infer geothermal gradient values of 19 °C km$^{-1}$, 29 °C km$^{-1}$, 43 °C km$^{-1}$, 85 °C km$^{-1}$, 44 °C km$^{-1}$, and 114 °C km$^{-1}$ for sites 990HT03, 1014HG10, 1014HL03, K8B-3295G, K8A-3289P, and K8B-3290P, respectively (Fig. 8). By fitting the temperature decay model, measured thermal conductivity shows values of 1.03 W m$^{-1}$ K$^{-1}$, 1.03 W m$^{-1}$ K$^{-1}$, 1.03 W m$^{-1}$ K$^{-1}$, 1.17 W m$^{-1}$ K$^{-1}$, 1.03 W m$^{-1}$ K$^{-1}$, and 1.17 W m$^{-1}$ K$^{-1}$ for sites 990HT03, 1014HG10, 1014HL03, K8B-3295G, K8A-3289P, and K8B-3290P, respectively, with an average value of 1.07 W m$^{-1}$ K$^{-1}$. Due to thermal conductivity misfit model at site 990HT03 and anomalously low thermal conductivity estimations at sites 1014HG10 and 1014HL03, thermal conductivity values at these sites were excluded from the analyses. As alternative, thermal conductivity value from site K8A-3289P was adopted for sites 990HT03, 1014HG10, and 1014HL03 due

**Fig. 6** Detailed BSRs depths in the study area based on 3D reflection seismic MCS937. Deeper BSRs are situated beneath the depocenter of basin, while shallower BSRs are widely dispersed below mud diapirs (marked by grey dash lines). Corresponding depth of BGHS for each site is inferred by the number (in meter) above sites symbol. Except for sites 1014HG10 and 990HT03, where BGHS depths exhibit deeper estimation compared to those of BSRs depths, the remaining sites suggest the inverse argument. The mud diapirs delineation (gray dash lines) refers to the work of Dirgantara et al. (2020). *mbsf* meter below seafloor
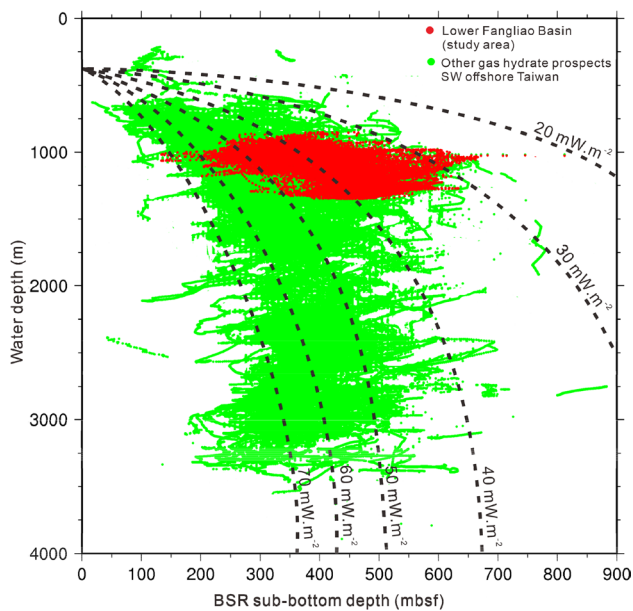
**Fig. 7** Cross plots of seafloor water depths versus BSRs sub-bottom depths both in upper slope and lower slope of accretionary wedge. Dashed curves are calculated gas hydrate stability curves for different theoretical heat flow values, assuming average seafloor temperature = 2.75 °C and average thermal conductivity of sediments = 1.00 W m$^{-1}$ K$^{-1}$ (Shyu et al. 2006; Liu et al. 2006). *mbsf* meter below seafloor

its close proximity to them. Heat flows, the product of geothermal gradients and thermal conductivities, suggest values of 19 mW m$^{-2}$, 29 mW m$^{-2}$, 44 mW m$^{-2}$, 99 mW m$^{-2}$, 45 mW m$^{-2}$, and 133 mW m$^{-2}$ for sites 990HT03, 1014HG10, 1014HL03, K8B-3295G, K8A-3289P, and K8B-3290P, respectively, with a mean value of 62 mW m$^{-2}$ and standard deviation of 44.05. Thermal conductivity based on infrared camera imaging infers increasing trend as the depth of penetration deepens, except at depth where sediment in core is absent (Fig. 10). Details regarding thermal properties of each site are presented in Table 1.

## Thermobaric model of hydrate stability zone

When information of water depth and seafloor temperature is present, BGHS can be modelled as an intersection of geothermal gradient and gas hydrate stability curve (Fig. 11). Normally, BGHS prediction requires seafloor temperatures information, which can be derived by extrapolating the geothermal gradient from direct measurement to the seafloor. However, since infrared thermal image was implemented on board, the seafloor temperature cannot be retrieved for this method. Instead, the seafloor temperatures of sites K8A-3289P and K8B-3290P refer to that of site K8B-3295G. Based on previous studies (Davis et al. 1990; Ganguly et al. 2000; Yang et al. 2004; Liu et al. 2006), lithostatic pressure condition
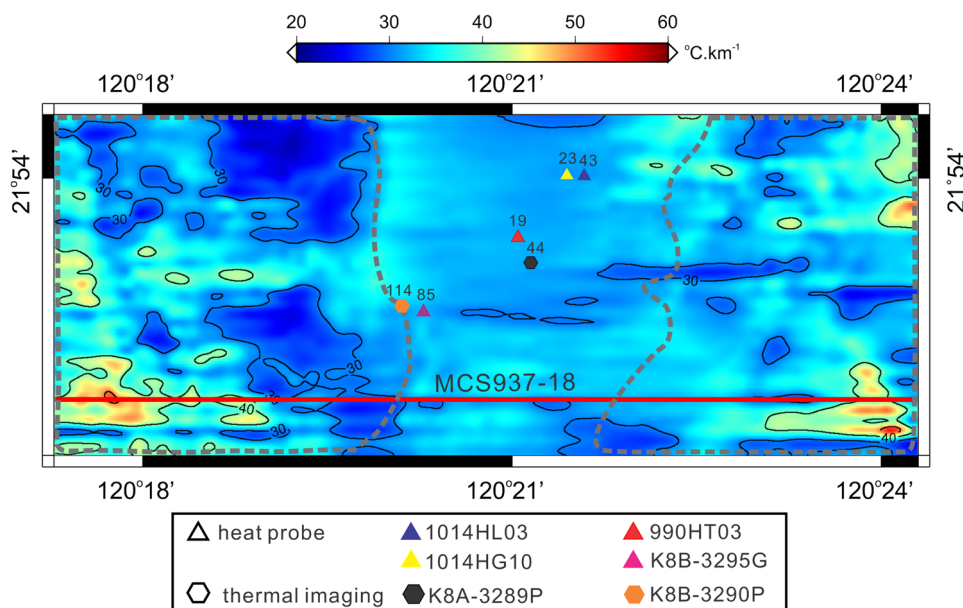


**Fig. 8** Geothermal gradient estimation from BSRs in the study area, with an average value of 33.12 °C km$^{-1}$. Relatively lower geothermal gradients dominate throughout the entire area, except some higher geothermal gradients distributed in the local area within mud diapirs domain. With an average value of 55 °C km$^{-1}$, corresponding direct measurement of geothermal gradients for each site is inferred by the number above site symbol. Only at sites 1014HL03, K8B-3295G, K8A-3289P, and K8B-3290P where the geothermal gradients from direct measurements are higher than the values of those derived from BSRs. The mud diapirs delineation (gray dash lines) refers to the work of Dirgantara et al. (2020)

**Fig. 9** BSRs-derived heat flows distribution map with an average value of 41 mW m$^{-2}$. Relatively low heat flow dominates majorly the entire area, while higher heat flows are locally linked to presence of mud diapirs. Corresponding direct measured heat flow for each site is inferred by the numbers above site symbol, giving a mean estimation of 62 mW m$^{-2}$. At sites 990HT03 and 1014HG10, direct measured-heat flows are lower than those estimated from BSRs. The mud diapirs delineation (gray dash lines) refers to the work of Dirgantara et al. (2020)
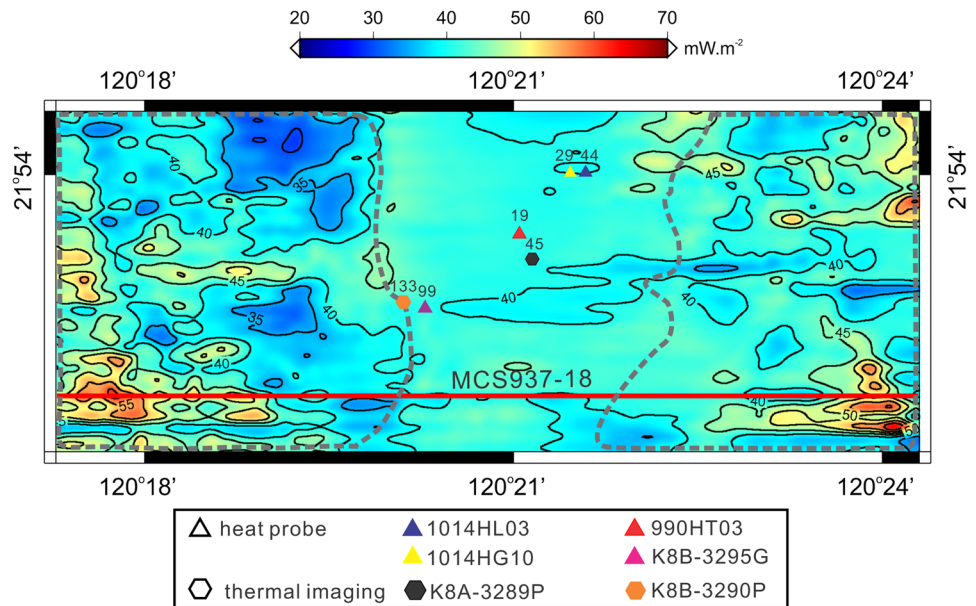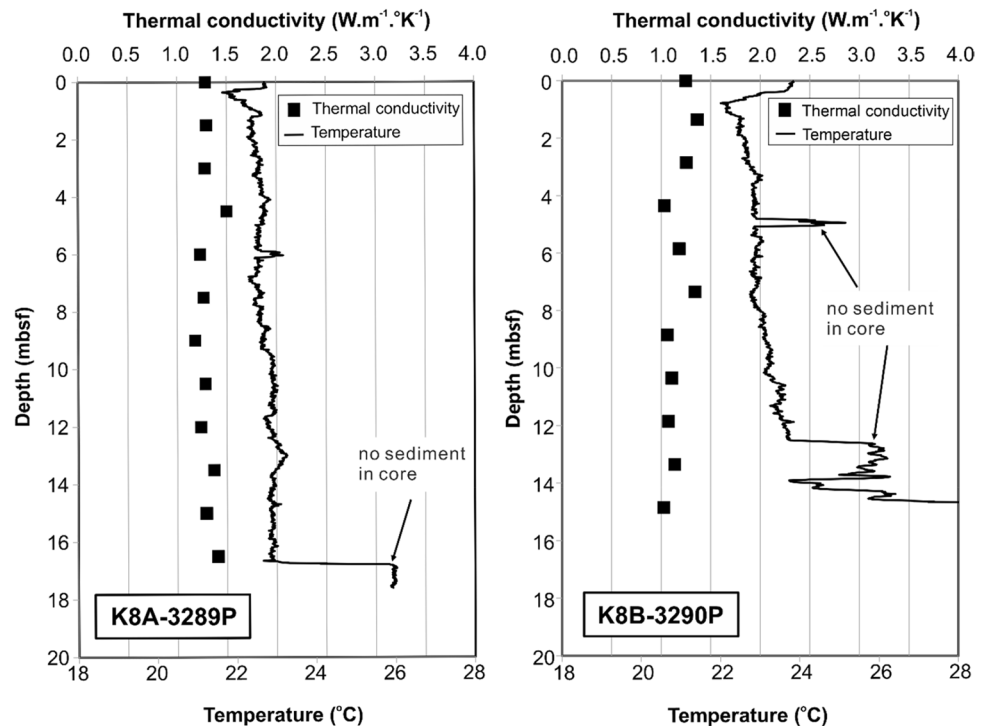


**Fig. 10** Measurement of thermal conductivity based on thermal probe and sediment core temperature based on infrared imaging for sites K8A-3289P and K8B-3290P. Increased thermal conductivity is related to empty cores in the core barrels. *mbsf* meter below seafloor.



with methane-dominant content is assumed to derive the gas hydrate stability curve. Results hint the BGHS spans at depths below seafloor around 828 m, 542 m, 326 m, 152 m, 314 m, and 311 m for sites 990HT03, 1014HG10, 1014HL03, K8B-3295G, K8A-3289P, and K8B-3290P, respectively, giving an average depth of 412 m below seafloor (Fig. 6; Table 1).

## Seismic interpretation

Gas-hydrate and free-gas systems of the study area have been advocated by Dirgantara et al. (2020), highlighting gas-hydrate and free-gas compartments based on seismic facies principle and seismic facies groups. On seismic line MCS937-18, the BSRs are situated underneath cut-and-fill facies (Fig. 12), where layers of high-amplitude

**Table 1** Compilation results of in-situ thermal measurement, thermal infrared imaging and BSRs-derived thermal properties

| Site name | Latitude | Longitude | Z (m) | $T_0$ (°C) | K (W/m K) | BGHS (mbsf) | BSRs (mbsf) | Diff (mbsf) | G (°C/km) | G' (°C/km) | Diff (°C/km) | Q (mW/m) | Q' (mW/m) | Diff (mW/m) |
|---|---|---|---|---|---|---|---|---|---|---|---|---|---|---|
| 990HT03 | 120.350 | 21.892 | 1287 | 3.63 | 1.03[a] | 828 | 480 | 348 | 19 | 31.75 | − 12.75 | 19[a] | 41 | − 22 |
| 1014HG10 | 120.357 | 21.899 | 1287 | 3.17 | 1.03[a] | 542 | 484 | 58 | 29 | 31.85 | − 2.85 | 29[a] | 40 | − 19 |
| 1014HL03 | 120.358 | 21.899 | 1283 | 3.17 | 1.03[a] | 326 | 485 | − 159 | 43 | 32.11 | 10.89 | 44[a] | 40 | 4 |
| K8B-3295G | 120.337 | 21.882 | 1284 | 3.29 | 1.17 | 152 | 472 | − 320 | 85 | 32.46 | 53.54 | 99 | 41 | 58 |
| K8A-3289P | 120.352 | 21.888 | 1284 | 3.29[b] | 1.03 | 314[b] | 495 | − 181 | 44 | 31.3 | 12.7 | 45 | 40 | 5 |
| K8B-3290P | 120.335 | 21.883 | 1282 | 3.29[b] | 1.17 | 311[b] | 476 | − 165 | 114 | 31.93 | 31.93 | 133 | 40 | 93 |

Thermal conductivity at site 990HT03 is unknown due to misfit of temperature decay curve. Thermal conductivities at sites 1014HG10 and 1014HG10 are excluded due to anomalously low values

Z water depth, $T_0$ seafloor temperature, K thermal conductivity, BGHS base of gas hydrate stability, BSRs bottom simulating reflectors, G measured geothermal gradient measurement, G' BSRs-derived geothermal gradient, Q measured heat flows, Q' BSRs-derived heat flows, Diff discrepancy between direct measurement and BSRs-derived thermal properties

[a] Refers to Q using K referring to of site K8A-3289P

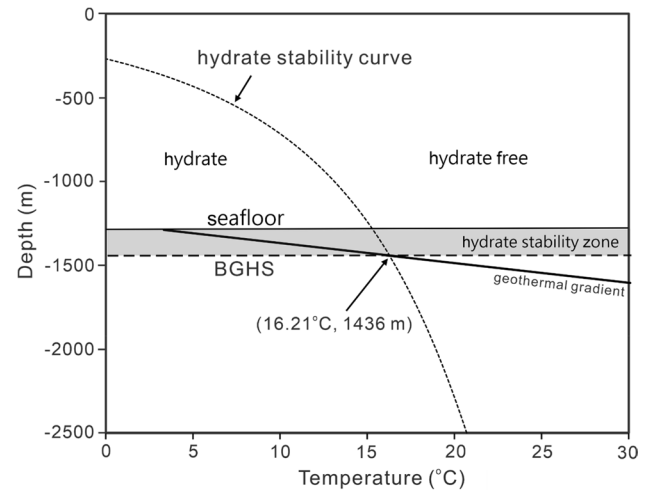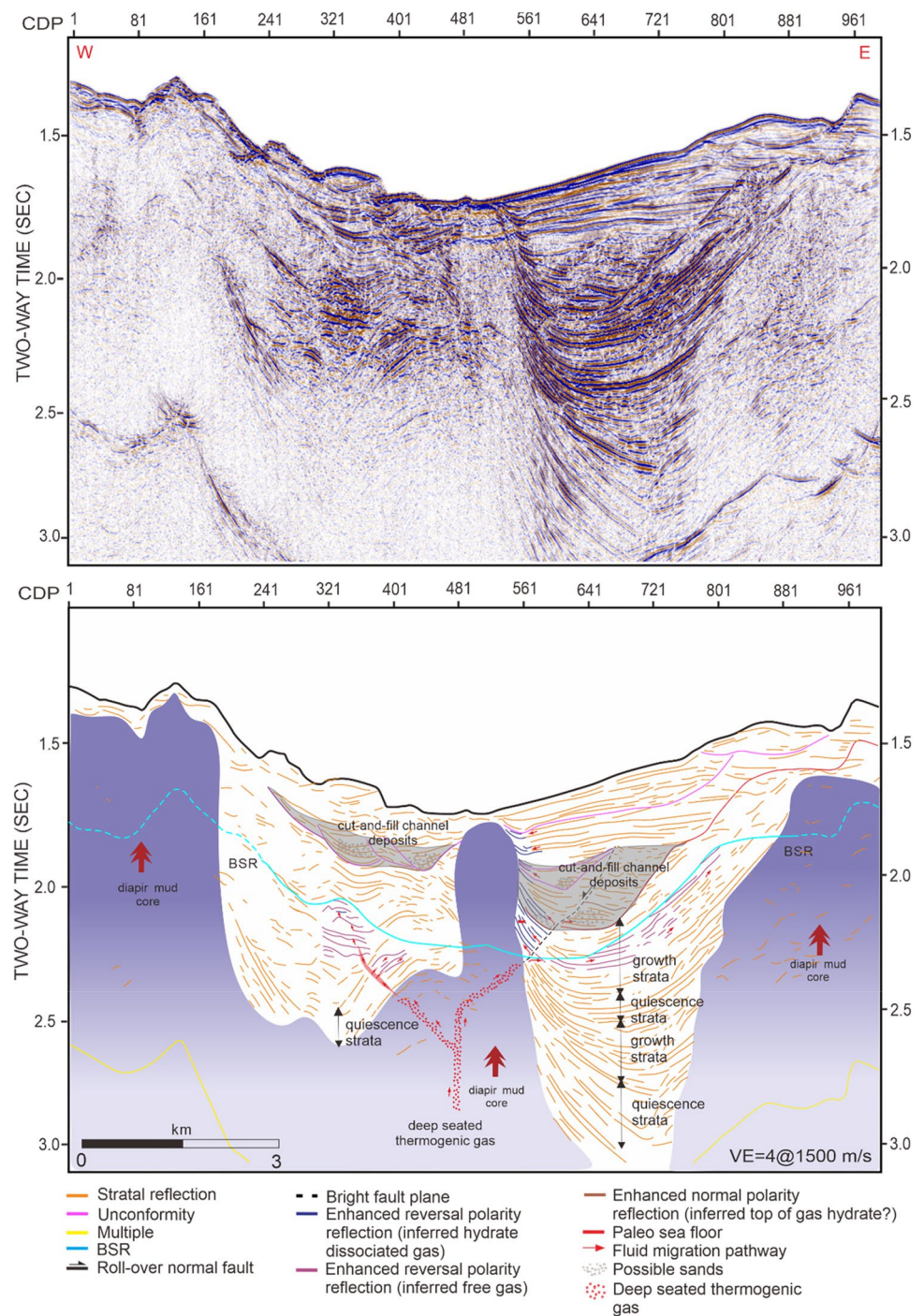[b] Refers to BGHS using $T_0$ referring to site K8B-3295G



**Fig. 11** An example of theoretical gas hydrate phase diagram derived from gas hydrate stability curve and geothermal gradient at site K8B-3290P. Base of gas hydrate stability is calculated at 1436 m water depth and sub-bottom temperature of 16.21 °C. Note that seafloor temperature of this site refers to site K8B-3295G due to the nature of infrared thermal image that was not capable to retrieve seafloor temperature

reflections confined in stacking series of bowl-shaped reflections are interpreted as cut and-fill-channels confining turbidite sands. Mud diapirs are inferred from their relatively free-reflection facies, indicating homogeneity within the mud body. Rim synclines at the base of the diapiric body with upturned sediment layers by the rising diapirs are present. Chen at al. (2014) suggested control of mud diapirism in shaping the morphology of the upper Gaoping Slope, highlighted by a series of structural highs and slope basins. These variations, in turn, contribute to major changes in sediment routes and distribution (Hsu et al. 2013; Hsiung et al. 2014).

Additional east-west trending seismic lines, MW9006-01 and MW9006-02, are interpreted to constrain the continuity of cut-and-fill facies. Both lines are situated to the northern part of the Lower Fangliao Basin, approximately 30 km and 15 km from MCS937-18, subsequently. While presence of BSRs is less clear, however, existence of cut-and-fill facies can be tracked down in both seismic lines. In MW9006-01 (Fig. 13), the cut-and-fill facies is situated to the east of Gaoping Canyon between two diapiric ridges. Episodic cutting and filling processes are present, where rapid slumps or slides deposition contributes to the migration of canyon thalweg westward (Liu et al. 1993). Both normal strata and growth strata are discernible, suggesting the dynamics of mud diapiric evolution through time. Normal strata marked quiescence deposition of inter-intrusive period, whereas growth strata hinted syn-depositional intrusion period (Dirgantara et al. 2020). On MW9006-02 (Fig. 14), double sided cut-and fill facies bounded by three diapiric ridges are

**Fig. 12** An example of gas hydrate and associated free gas systems in the study area from the MCS937-18 2D line. Above and below figures are uninterpreted and interpreted profiles. Cut-and-fill channel facies are shaded under translucent grey area. Refer to Fig. 2 for line location. *CDP* common depth points, *VE* vertical exaggeration, *W* west, *E* east. Modified from Dirgantara et al. (2020).



observable. The canyon wall is widening by oversteepening, sliding, and slumping accompanied by several stages of erosion and deposition (Liu et al. 1993).

## Discussion

### Parameter errors

Equation 1 infers the strong influences of both thermal conductivity and geothermal gradient on parameter errors for heat flow estimation and measurement. Inevitably, both methods possess source of errors due to their limitation. Heat flows from BSRs were calculated mostly based on

**Fig. 13** Uninterpreted (above) and interpreted (below) reflection seismic sections from the MW9006-01 line. The seismic line is located 30 km to the north from the 3D MCS937 seismic data. Cut-and-fill channel facies is discernible, inferring the possible last stage of paleo-Gaoping canyon prior to blockage. Refer to Fig. 2 for line location. *CDP* common depth points. *VE* vertical exaggeration, *W* west, *E* east
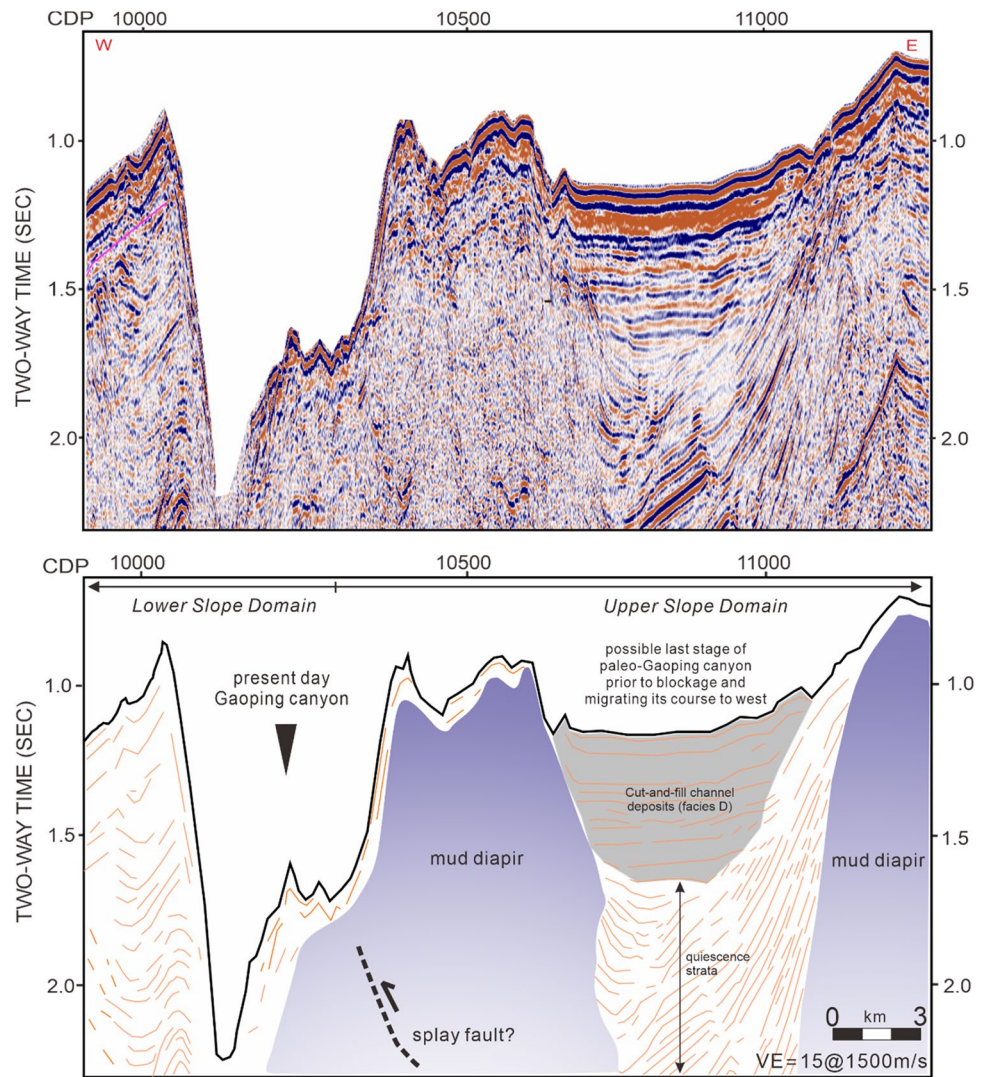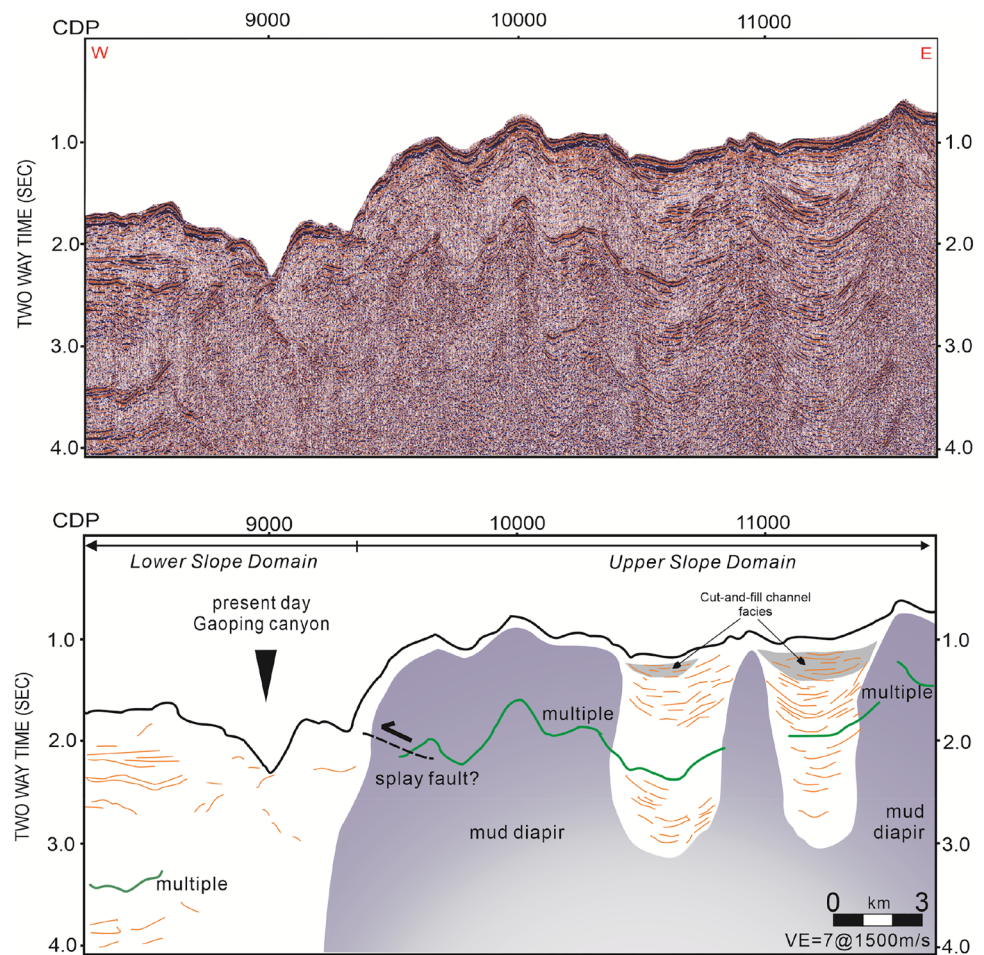
experimental approaches (e.g. Davis et al. 2000; Ganguly et al. 2000), where each of the corresponding approach is constrained by certain boundary conditions and assumptions. Time-to-BSRs depth conversion from seismic data produces error less than 3% (Davis et al. 2000) and lithostatic pressure model contributes an error of 12% (Ganguly et al. 2000). On the other hand, direct thermal measurement is hindered by limited probe penetration depth while the subsurface temperature is far from steady state assumption, thus vague linear geothermal gradient extrapolation may prevail. Geothermal gradient based on thermal imaging assumes uniform temperature increment during core recovery which may be invalid as the temperature disturbance at the time of penetration and thermal background during core recovery may not be uniform. The diurnal or seasonal variations of bottom water temperature are surmised to only affect the subsurface temperature by an amplitude with exponential decay with depth. This assumption neglects the possible influence of long

period oscillation of temperature variation on water bottom temperature. Although the thermal probe measurements were carried out in water depth greater than 1200 m, large variations of deep bottom water temperature in the western Pacific region have been reported by Kawano et al. (2006, 2010). Under steady state conduction, geothermal gradients from both BSRs estimation and direct thermal measurement shall exhibit fairly close values. However, Eq. 6 infers depth-dependence of thermal conductivity, hence discrepancy values between both methods are expected. Thermobaric model for pure water or saline with various gas compositions delivers errors in the range of 5–20% (Davis et al. 1990; Ganguly et al. 2000; Hyndman et al. 1992). These combined factors lead to the deviation between BSRs-derived heat flows and direct heat flows measurement by the margin of 10% in Makran accretionary prism (Kaul et al. 2000) and 30% in the Nankai Trough (Ashi and Taira 1993).

**Fig. 14** Seismic reflection for both uninterpreted (above) and interpreted (below) sections from the MW9006-02 line. Situated 15 km to the north from the 3D MCS937 seismic data, this seismic profile infers the presence of double sided cut-and fill facies bounded by three diapiric ridges. Refer to Fig. 2 for line location. *CDP* common depth points, *VE* vertical exaggeration, *W* west, *E* east

## Discrepancies between BSRs-derived thermal properties and direct thermal measurement

Depth of BSRs are generally deeper than BGHS, except for sites 990HT03 and 1014HG10 (Fig. 5), with difference from −320 to 348 m and an average difference of −70 m. Negative values indicate deeper depth of BGHS than BSRs. Since geothermal gradients are extrapolated using linear gradient from seafloor downward, except for sites 990HT03 and 1014HG10, geothermal gradient estimation from BSRs are generally lower than the measured ones (Fig. 8). Difference between these two ranges from −12.75 to 82.07 °C km$^{-1}$, with a mean value of 23 °C km$^{-1}$. Estimation of heat flows from BSRs and direct heat flows measurement suggests an average difference of 21 mW m$^{-2}$, spanning from −21.45 to 92.65 mW m$^{-2}$. This suggests how BSRs-derived heat flows are generally lower than measured heat flows, except for sites 990HT03 and 1014HG10 (Fig. 9) where the geothermal gradient values are lower. The smaller standard deviation in BSRs-derived heat flows (4.57) than that of the measured heat flows (44.05) suggests less variation in heat flows estimated from BSRs is present than that in measured heat flows. A general trend of increasing temperature with

depth on the thermal images is found for sites K8A-3289P and K8B-3290P. Abrupt changes in geothermal gradient responses are related to empty core in the core barrel and allow trapped air to be heated easily, hence higher temperature records (Fig. 10). Table 1 compiles the differences between two methods.

## Geological constraints of thermal estimation from direct measurements

Under similar direct thermal measurement approach, Shyu et al. (2006) calculated the BSRs depths in the northeastern side of the Lower Fangliao Basin to be 16% deeper than that of measured BGHS depth. This argument is consistent with this study, where BGHS depths are shallower than BSRs depths (Table 1) with discrepancy margin of 70%. Using analytical formulation, Xu and Ruppel (1999) postulated that BGHS can only be treated as the base of hydrate occurrence if mass of methane dissolved in liquid exceeds methane solubility in seawater and if the methane flux carried by porous water flow exceeds a critical value corresponding to the rate of diffusive methane transport. While BSRs represents the sudden drop in acoustic impedance

between overlying hydrates and underlying free gas (Zhang and McMechan 2006), in some cases, free gas zone can be separated from overlying hydrate occurrence and BGHS by intervening sediment layer that contains neither hydrate nor free gas (Xu and Ruppel 1999), where BSRs may occur deeper than BGHS.

Other than capillary effect (Handa and Stupin 1992), focused fluid flow (Davis et al. 1990), gas composition (Waseda and Uchida 2004), and interstitial water chemistry (Lu and Matsumoto 2001), discrepancies between BSRs-derived heat flows and direct heat flows measurement can be subject to topography effect (Dong et al. 2008). In the Shenhu gas hydrate prospect, northern slope of the South China Sea, changes in 142 m of bathymetry level contribute to 50% error margin of measured heat flows (Dong et al. 2008). In this study, direct thermal measurement in a relatively flat basin depocenter with water depth variation of ~ 5 m (Fig. 3 and Table 1). This suggests topography effect is most likely minor in the area while those measured sites are not far away from each other. Davis et al. (1990) suggested focused fluid flow along shallow fractures and faults contribute indirectly to the heat flow disparity. Direct thermal measurement was carried out mainly in the basin depocenter, where low migration rate of 6 cm year$^{-1}$ (Chen et al. 2012), thick hemipelagic facies, and scarcity of shallow faults (Dirgantara et al. 2020) were suggested in the Lower Fangliao Basin. These suggest focused fluid flow through structural pathways is unlikely to control the heat flow variation. Alternatively, influence of shallow fluid flux was proposed by Dong et al. (2008) to control the heat flow variation at deeper and shallower strata. Fluid flux contributes to elevated geothermal gradient as the fluid migrates upward (Xu and Ruppel 1999). As result, geothermal gradients remain low for deeper strata compared to higher geothermal gradients near the seafloor. Thermal probe measurement only quantifies the higher geothermal gradient zonation close to the seafloor, hence higher heat flow values. Wang et al. (2005) concluded wide difference (−87 to 59%) between measured heat flows and BSRs-estimated heat flows in the

northern margin of South China Sea. In this study, wider heat flow difference (−109 to 69%) is present. Shyu et al. (2006) estimated at least 15% of average heat flows estimated from BSRs depth were lower than that of measured heat flows in the northeastern bound of the Lower Fangliao Basin. This agrees with results of this study, where heat flow values from measurement are higher than BSRs-calculated heat flow values (Table 1) with average discrepancy margin of 21%.

Sedimentation rate in the study area is estimated to be around 0.7 to 4.5 mm year$^{-1}$ (Lin et al. 2014; Yu et al. 2017) with the development of slope basins began since ~ 1.8 Ma (Hsu et al. 2017). Based on Eq. 8, corrected geothermal gradient and heat flow can be elevated by order of 52% and 37,847% for sedimentation rate of 0.7 mm year$^{-1}$ and 4.5 mm year$^{-1}$, respectively (Table 2). These infer if the sedimentation rate varies over the past 1.8 Ma and corrected amount is sensitive to the thermal conductivity. Using 0.7 mm year$^{-1}$ correction, the average measured heat flows rise to 93 mW m$^{-2}$. Shyu et al. (2006) showed correction of 10% contribute for sedimentation rate of 0.3 mm year$^{-1}$ in the Gaoping Slope. Under the aforementioned sedimentation rate, correction of geothermal gradients up to 10–40% in study area is reasonably expected.

## Geological constraints of thermal estimation from BSRs

Catalogue based on relationships between BSRs distribution, submarine topography, and tectonic features in off southwestern Taiwan infer both ridge type-BSRs and basin-type BSRs to be present in the study area (Lin et al. 2009b). While BSRs are vivid beneath the crest of anticlinal mud diapirs, discernible BSRs are also present at the basin margin and within the basin depocenter (Figs. 4; 12). Along the basin margin, BSRs are depicted by reversal polarity reflection cutting sub-parallel strata. BSRs within the basin interior are difficult to distinguish, as stratal reflections are often parallel to the seabed. In general, BSRs are more or

**Table 2** Comparison of geothermal gradient and heat flow corrections under sedimentation rate of 0.7 mm year$^{-1}$ and 4.5 mm year$^{-1}$

| Site | $G$ (°C km$^{-1}$) | $G_{C1}$ (°C km$^{-1}$) | Diff (°C km$^{-1}$) | $G_{C2}$ (°C km$^{-1}$) | Diff (°C km$^{-1}$) | $Q$ (mW m$^{-2}$) | $Q_{C1}$ (mW m$^{-2}$) | Diff (mW m$^{-2}$) | $Q_{C2}$ (mW m$^{-2}$) | Diff (mW m$^{-2}$) |
|---|---|---|---|---|---|---|---|---|---|---|
| 990HT03 | 19 | 27 | 8 | 283 | 264 | 19 | 28 | 9 | 291 | 272 |
| 1014HG10 | 29 | 54 | 25 | 7682 | 7653 | 29 | 56 | 27 | 7912 | 7883 |
| 1014HL03 | 43 | 97 | 54 | 120,424 | 120,381 | 44 | 100 | 56 | 124,037 | 123,993 |
| K8B-3295G | 85 | 115 | 30 | 878 | 793 | 99 | 134 | 35 | 1,023 | 924 |
| K8A-3289P | 44 | 62 | 18 | 608 | 564 | 45 | 63 | 18 | 626 | 581 |
| K8B-3290P | 114 | 155 | 41 | 1177 | 1063 | 133 | 181 | 48 | 1377 | 1244 |

$G$ original thermal gradient, $G_{C1}$ thermal gradient correction with sedimentation rate 0.7 mm year$^{-1}$, $G_{C2}$ thermal gradient correction with sedimentation rate 4.5 mm year$^{-1}$, $Q$ original heat flow, $Q_{C1}$ heat flow correction with sedimentation rate 0.7 mm year$^{-1}$, $Q_{C2}$ heat flow correction with sedimentation rate 4.5 mm year$^{-1}$, Diff discrepancy between original thermal values and corrected thermal values

less parallel to the seafloor and exhibit increasing depth with water depth (Shyu et al. 2006). The absence of BSRs in some parts of the studied seismic profiles infer intrinsic circumstances governing the formation mechanism of BSRs. Since BSRs mark the sub-bottom depth where the geothermal gradient intersects the methane-hydrate-water equilibrium curve (Dickens and Quinby-Hunt 1997), internal factors may contribute to the perturbation of BSRs formation, e.g saturation and distribution of gas hydrates in pores (Tinivella and Lodolo 2000), volume of free gas (Zhang et al. 2012), water salinity (Clennell et al. 1999), and wettability of sediment host (Sloan and Koh 2007). Hillman et al. (2017) viewed the distribution of discontinuous BSRs as patches or segmented reversed polarity reflection, yet still simulates the sea-floor reflector trend. Nevertheless, hydrate-bearing sediments have been proven to exist without the presence of BSRs, as in the Peru margin (Kvenvolden and Kastner 1990) and the Blake Ridge (Tinivella and Lodolo 2000; Holbrook 2001). In the lower accretionary wedge off southwestern Taiwan, discontinuous BSRs have been credited to the upward flow of under-saturated fluid which depletes free gas faster than gas produced by hydrate recycle (Lin et al. 2009b). Albeit the non-existence of BSRs in some part of the study area, this study supports the likelihood of gas hydrate over free gas as proposed by previous studies (Hsu et al. 2017; Dirgantara et al. 2020).
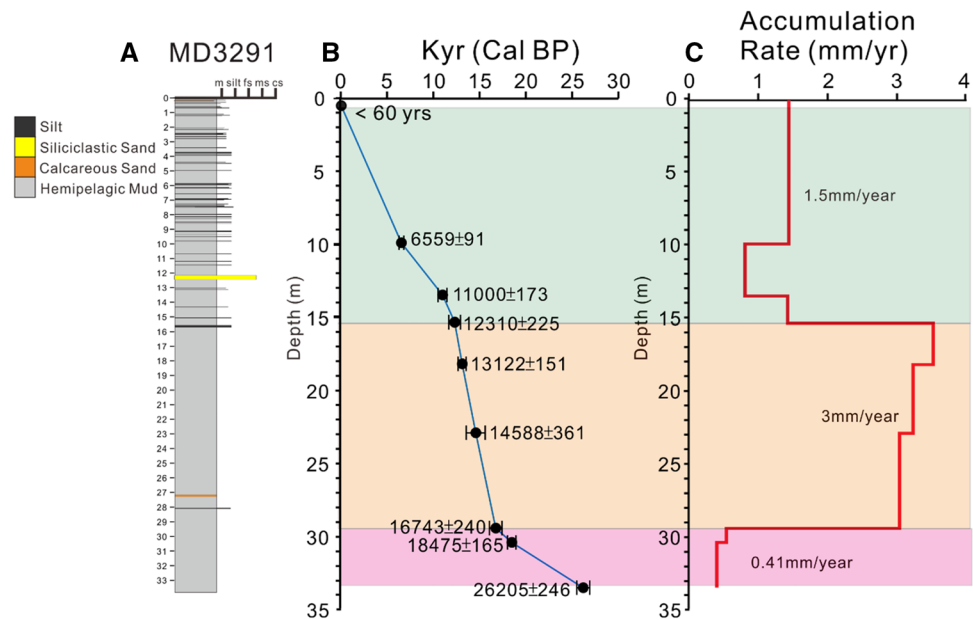
In addition to pressure, other variable that affects the stability of gas hydrates is temperature. Variations of BSRs sub-bottom depths are highly prone to the dynamic of pressure and temperature conditions in subsurface. In the effort of estimating heat flow from BSRs, it is a challenge to precisely measure the thermal properties. However, the geothermal gradients will change in an order of less than 2.5 °C km$^{-1}$ for an arbitrary 30% error in estimating BSRs depth (Chi and Reed 2008). In offshore southwestern Taiwan, BSRs depths exhibit shallowing depth trend as it transcends from lower slope to upper slope (Fig. 3). Nonetheless, in the study area, depths of BSRs are generally deeper than the background BSRs depths in the upper wedge slope. Such condition can be linked indirectly to the heat flow values within the area, where spatial distribution of heat flows infers relatively lower values (41 mW m$^{-2}$) as opposed to average heat flows in submarine accretionary wedge of Taiwan (43 mW m$^{-2}$ to 64 mW m$^{-2}$) reported by previous studies (Shyu et al. 2006; Chi and Reed 2008). Relatively low heat flow values infer prominent thermal sealing capacity in the study area (Fig. 9).

Influence of mud diapirs with respect to thermal properties exhibits different behaviours depending on constituents within the diapirs themselves. In the South Caspian Basin, mud diapirs are noted for their massively gas-charged bodies with low thermal conductivities (Bagirov and Lerche 1997). In the Mediterranean Ridge accretionary complex, relatively low heat flow values ranging between 16 and 41 mW m$^{-2}$

have been reported (Camerlenghi et al. 1995), inferring a rather cold conductive thermal regime operating within the area. In contrary, influence of mud diapirs toward increment of geothermal gradients is attributed to upward migration of warm fluids from deeper region in accretionary complex of Barbados ridge complex (Davis and Hussong 1984), where heat flows on active mud diapirs are higher than that of the surrounding basin and appears to have derived from over-pressured fluid beneath the Barbados accretionary prism (Henry et al. 1990). Thermal probe measurements in the upper slope off southwestern Taiwan inferred a group of high heat flow values (76 to 170 mW m$^{-2}$) on the summit of mud diapirs, accompanied by a lower heat flow measurement (55 mW m$^{-2}$) on the diapir flank (Shyu et al. 1998). The high heat flow anomalies can be explained by assuming a continuing seepage of warm fluid through the seafloor on active mud diapirs (Langseth et al. 1988), whereas the low heat flow variation can be related to gas infilled mud diapirs (Shyu et al. 1998). The spatial variations of geothermal gradients estimated from BSRs do not exhibit correlation with seafloor bathymetry (Fig. 8), yet BSRs-derived heat flows are locally high in the southwestern, southeastern, and northeastern parts of the study area, where mud diapirs are present (Fig. 9). These suggest subsurface thermal perturbation may prevail locally within the current non-active phase of mud intrusions.

In addition to geothermal gradient perturbation, rapid sedimentation rate may also affect the thermal field within a basin. Significant reduction level of basin temperature is commonly reduced by thermal blanketing effect introduced by rapid sedimentary accumulation (Lucazeau and Le Douaran 1985; Bjorlykke 2010). This phenomenon occurs when thermal effect of cold sediments deposition on top of the lithosphere leads to a depression of local geothermal gradient. In the Pliocene-Pleistocene Coastal Range of eastern Taiwan, high percentages of smectite at 6 km depth are interpreted as a result of high sedimentation rates (> 5 km M year$^{-1}$) and kinetic limitations, which promotes a low paleo-geothermal gradient of 14 °C/km (Dorsey et al. 1988). Furthermore, high sedimentation rates (~ 1 mm year$^{-1}$) and rapid subsidence are capable to induce cooling effect and perturb the transient thermal nature by reducing the heat flow level in order of 10–20%, taking more than 30 M year to restore the normal heat flux background (Husson and Moretti 2002). During late Pliocene-Holocene, under-filled foreland basins bordered by a relatively narrow shelf and broad wedge slope have been resulted from sediments deposition of the Taiwan orogen infilling the deep marine basin in the northeastern South China Sea (Yu 2004). With an average sedimentation rate of 0.7–4.5 mm year$^{-1}$ (Lin et al. 2014; Yu et al. 2017), at least 6.6 M tons per year of sediment have been deposited in the slope off Taiwan (Huh et al. 2009). Recent sedimentation rate study within the vicinity

**Fig. 15** **a** Graphic sedimentological logs for MD3291; **b** age (AMS 14C dating) and depth relationship; **c** variations of sediment accumulation rate through time. Refer to Figs. 1 and 2 for core location. Modified from Yu et al. (2017)

of the Lower Fangliao Basin can be inferred from MD3291 coring (Fig. 15). The sediment core is situated to the west of the lower slope of Gaoping Canyon with bathymetry depth of 600 m shallower than the depth of Gaoping Canyon thalweg (Figs. 1, 2). Yu et al. (2017) inferred rate of sediment accumulation at this site varies from 0.41 to 3 mm year$^{-1}$ in the last 26 k year (Fig. 15). Approximately 6000 m sediment thick have been piled up in the southwestern foreland basin and accumulated on the slope off southwestern Taiwan (Covey 1984). High sedimentation rate of an accretionary wedge bordering mountain belts is a common characteristic shared by active margins. In the Makran wedge, a sediment mass accumulation of around 350 km$^3$ was found for a 1 km wide area along the trench basin (Fruehn et al. 1997). Thus, a high sedimentation rate in active convergent margin may contribute to the thermal blanketing effect, such as the case in the study area.

Based on bathymetry information (Fig. 2), the Lower Fangliao Basin can be considered to be the final depositional pathway of Fangliao Canyon before it merges with the Gaoping Canyon along the splay fault. Morphology of the Lower Fangliao Basin merges from two submarine drainage systems: the eastern drainage, where the current Fangliao Canyon distributes, and the western drainage, where narrow inactive submarine channel occupies. While the eastern drainage has more active sediment supply, the study area is situated at the western drainage where no active erosive processes are present. Since the BSRs are situated at the depth below cut-and-fill facies in the basin depocenter (Fig. 12), it is inferred that sediment history plays a cardinal role in controlling the present heat flux. The paleo-canyon had deposited a stack series of water-saturated and high porosity turbidite sands. Rapid deposition rate in offshore

southwestern Taiwan had caused insufficient dewatering process in the paleo-canyon sediments, leaving high water saturation within pore spaces. Besides affecting the strength of sediments, the trapped pore waters may also lower the bulk thermal conductivity. Such phenomenon is linked to the deepening base of GHSZ. This base also marks the incipient increment of geothermal gradients underneath the anomalous zone, where the geothermal gradients may begin to revert to the background values. Vast discrepancies between heat flow values in the Lower Fangliao Basin versus neighbouring gas hydrate potential area infer wide spectrum of heat flow distribution in the study area (Fig. 7).

## Evolution of the Lower Fangliao Basin Off southwestern Taiwan

Regional basin evolution offshore southwestern Taiwan exerts a primary control on the thermal properties anomaly and the development of mud diapirs and gas hydrate in the upper accretionary wedge through time. Generally, the origin of submarine canyon can be related to river incision, subaerial erosion, turbidity currents erosion, structural movements, and biological activities (Yu and Lu 1995). Regional framework in southwestern Taiwan, including offshore areas, was established during the Pliocene-Quaternary (Covey 1984). Genetic relationship between offshore mud diapirs and onshore mud volcanoes in southwestern Taiwan has been discussed by previous geochemistry studies (Yu et al. 2004; Sun et al. 2010). Yang et al. (2011) proposed offshore mud diapirs/mud volcanoes relationship with onshore mud volcanoes as an accretionary wedge conveyor belt. Filling-and-spilling processes have been proposed by previous authors (Yu and Huang 2006; Hsu et al. 2013) for

describing sediment dispersal and accumulation in Gaoping Slope basins. Hsu et al. (2017) has suggested eight stages of the Lower Fangliao Basin development through time. This approach, however, does not take into account the influence of paleo-canyon deposition towards present day thermal anomalies within the basin. Therefore, an alternative model is proposed.

The cut-and-fill channel facies (Figs. 12, 13, 14) can be interpreted as remnant deposition of paleo-Gaoping canyon prior being intruded by mud diapirs, as inferred from bathymetry data, facies interpretation, and heat flow anomalies. Extensive development of mud diapirs have blockaded the paleo-canyon and diverted it to the present Gaoping Canyon course (Fig. 1), In the bathymetry map, a ridge has blockaded the original south canyon course, diverting it to the SW direction at about 22° 16′ N (Fig. 2). From this bend, the canyon run south-westward until it turned south-eastward following the strike of west-vergent splay fault. This premise was supported by Sun and Liu (1993), who inferred the paleo-submarine canyon of the study area as an old Gaoping canyon and later abandoned due to the rise of mud diapirs. Hsu et al. (2017) proposed the diapiric activities to cause slope readjustment, modify morphological features, and affect sediment transport processes in upper Gaoping Slope. Intrusion of ductile materials to the diversion of

submarine canyon has been reported elsewhere. Yu and Lu (1995) proposed an uplifted mud volcano to bend the Upper Fangliao Canyon, similar to evaporitic bodies have caused a sharp bend of the Var Canyon in the Liguro-Provencal Basin (Pautot et al. 1984).

During late Miocene, the study area was under passive continental margin setting (Teng 1990), where mainly clay-rich sediments were deposited along the passive margin (Fig. 16a). Steady sedimentation leads to the increasing compaction, expulsion of pore water fluids, thermal maturation of organic matters, and reduction of porosity and permeability. Early Pliocene marked the onset of collision between N–S trending Luzon volcanic arc of the Philippine Sea Plate versus NE–SW trending passive continental margin of the Eurasian Plate (Lin and Watts 2002). This period marks the early transition from passive continental margin setting into peripheral foreland basin setting. The collision initiates the deformation of previously preserved passive margin sedimentation into intraslope basins simultaneously (Lin et al. 2003). Deep marine environment of offshore southwestern Taiwan progressively became nearshore and shallow marine depositional environments. Proto-orogen began to exhume in the southwestern direction starting from northern paleo-Taiwan. This shortening is the primary factor controlling structural evolution for the
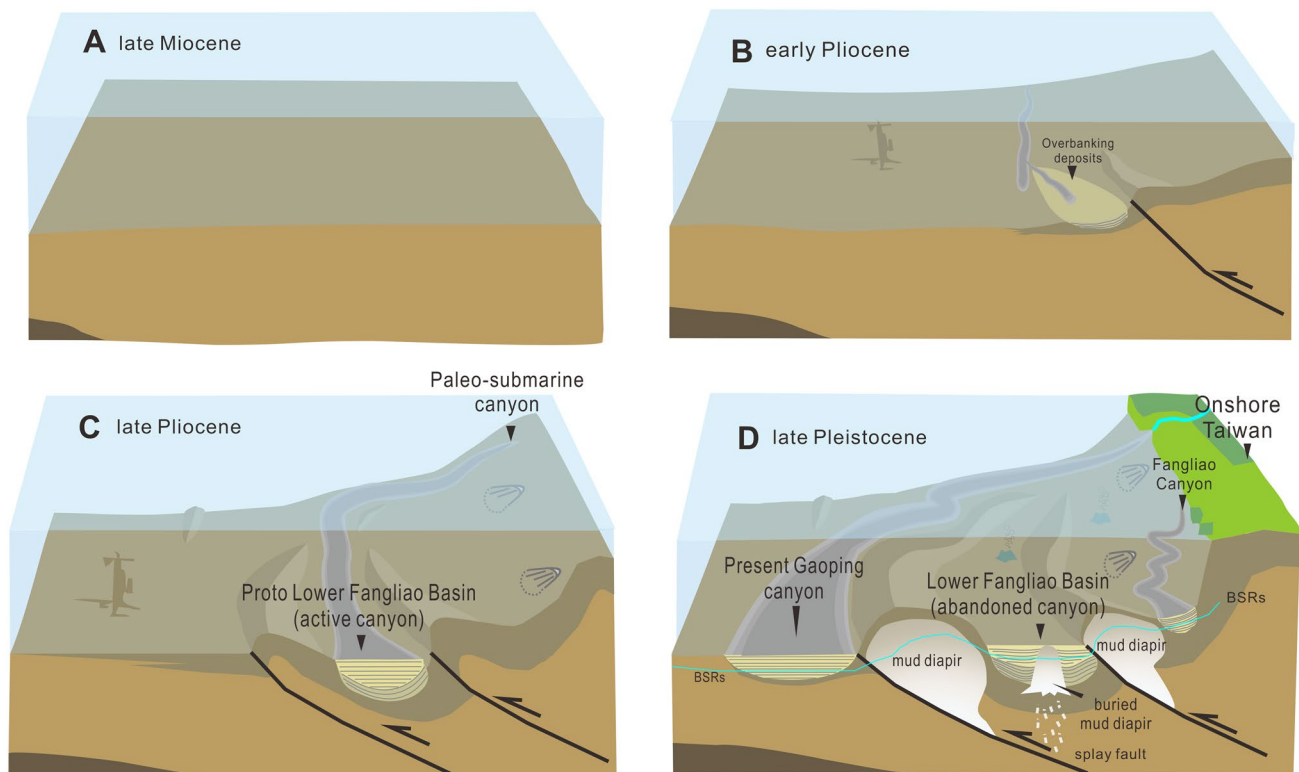


**Fig. 16** Schematic drawings showing the development of the Lower Fangliao Basin. **a–d** indicates the time during late Miocene, early Pliocene, late Pliocene, and late Pleistocene, respectively. Note that each figure is not to scale.

later mud intrusion. The first paleo-channel may have deposited overbanking sediments at the base of proto Lower Fangliao Basin (Dirgantara et al. 2020) (Fig. 16b). During late Pliocene, nascent Taiwan orogen was intensively accreted. Lithospheric flexure due to orogenic loading initiates the extensive development of west vergent and thrust-related anticlines. As opposed to Hsu et al. (2017), who proposed the submarine anticlines in southwestern offshore Taiwan as mud diapirs due to the presence of unbalanced sedimentary loading, this study asserts the submarine ridges in the upper slope of Taiwan accretionary wedge commenced as thrust-related anticlines and bordered the slope basin. Thick sequences of deep marine sediments filled the foredeep basin, mainly by the Pliocene-Pleistocene mud (Fig. 16c). The thick muddy sediments provide source material of later mud diapirs and overlaid with rapid shedding of orogenic sediments. During this stage, paleo-Gaoping canyon began to develop following the strike of slope basins. The canyon had deposited a series of active cut-and-fill facies overlying the previously preserved overbanking sediments (Dirgantara et al. 2020). Paleo-Gaoping canyon had flowed through the Lower Fangliao Basin following the strike of slope basin and deposited a stacked series of turbidite sands. During the early Pleistocene, the increasing burial depth causes an increase in burial stresses and temperature, leading to a decrease in porosity, and the catagenesis stage in the slope basin. Thermal maturation produces a series of progressively small hydrocarbon molecules of increasing volatility and hydrogen content, culminating with methane gas (Tissot and Welte 1984). Water-rich and organic-rich marine sediments experience tectonic stress and are incorporated into accretionary wedges, which later imbricated and thrusted as compressional belts (Brown and Westbrook 1988). Late Pleistocene marked the recent on-going arc-continent collision. Peripheral foreland basins are still developing to the western part of the orogen. Coupled with the on-going west vergent thrust-folds and upward migration of deep seated thermogenic gas, the increasing overburden stress promotes the initiation of submarine mud diapirism or mud volcanoes from previously preserved mud formation (Fig. 16d). Most of the mud diapirs extend in a NNE-SSW direction, similar to the trend of the folds onshore southwestern Taiwan (Lacombe et al. 2004). Trapped pore water and expulsion of hydrocarbon gas promote pore pressures soon to exceed hydrostatic and mud is overpressured. Due to density transposition, the mud may slowly ascend through the overburden rocks as mud diapirs and mud volcanoes. Buried mud diapirs may develop when mud intrusion does not significantly penetrate the seafloor. The trapped pore waters from rapid deposition and sediment burial lead to lowered sediment thermal conductivities, while rapid sediment burial results in insufficient time to adapt to the heat flow regimes. These, together, lead to lowered heat flows and thermal gradients

and contributes to deepen the base of GHSZ. Mud diapiric intrusions and uplifting of seafloors had blocked the course of paleo-Gaoping canyon. Finally, the Lower Fangliao Basin was abandoned following the canyon course shifted it to the south along the present-day Gaoping Canyon course.

## Conclusions

1. Estimated BSRs-derived geothermal gradients infer average value of 33 °C km$^{-1}$, while estimated heat flows infer an average value of 41 mW m$^{-2}$.
2. Direct thermal measurement by heat probe and thermal imaging from sediment cores suggest average geothermal gradients and heat flows of 55 °C km$^{-1}$ and 62 mW m$^{-2}$, respectively.
3. Discrepancies between both measurements are related to shallow heat flux, where shallow geothermal gradients elevate locally as the fluid migrates upward.
4. Rapid deposition and sediment burial in offshore southwestern Taiwan had caused insufficient dewatering process in the paleo-channel sediments, leaving high water saturation within pore spaces and hence overpressured sediments. The trapped pore waters lead to lower sediment thermal conductivities and rapid sediment burial results in insufficient time to adapt to the heat flow regimes. These, together, lead to lower heat flows and thermal gradients. This phenomenon contributes to deepen the base of gas hydrate stability zone in the Lower Fangliao Basin.

## References

Allen PA, Allen JR (2013) Basin analysis—principles and application to petroleum play Assessment. Wiley, Oxford

Ashi J, Taira A (1993) Thermal structure of the Nankai accretionary prism as inferred from the distribution of gas hydrate BSRs. Special Paper of the Geol Soc Am 273:137–149

Bagirov E, Lerche I (1997) Hydrates represent gas source, drilling hazard. Oil Gas J 95:99–101

Bjorlykke K (2010) Petroleum geoscience: from sedimentary environments to rock physics. Springer, London

Blackwell DD, Steele JL (1989) Thermal conductivity sedimentary rocks: measurement and significance. In: Naeser ND, McCulloh TH (eds) Thermal history of sedimentary basins: methods and case histories. Springer, New York, pp 13–36

Brown K, Westbrook GK (1988) Mud diapirism and subcretion in the Barbados Ridge accretionary complex: the role of fluids in accretionary processes. Tectonics 7:613–640

Bullard EC (1954) The flow of heat through the floor of the Atlantic Ocean. Proc R Soc Lond 222:408–429

Camerlenghi A, Cita MB, Vedova BD, Fusi N, Mirabile L, Pellis G (1995) Geophysical evidence of mud diapirism on the Mediterranean Ridge accretionary complex. Marin Geophys Res 15:115–141

Carslaw HS, Jaeger JC (1959) Conduction of heat in solids. Oxford University Press, London

Chen L, Wu CC, Liu CS, Shyu CT, Wang Y, Lu CY (2012) Deriving regional vertical fluid migration rates offshore SW Taiwan using bottom-simulating reflectors. Marin Geophys Res 33:379–388

Chen SC, Hsu SK, Wang Y, Chung SH, Chen PC, Tsai CH, Liu CS, Lin HS, Lee YW (2014) Distribution and characters of the mud diapir and mud volcanoes off southwest Taiwan. J Asian Earth Sci 92:201–214

Chi WC, Reed DL (2008) Evolution of shallow, crustal thermal structure from subduction to collision: an example from Taiwan. Geol Soc Am Bull 120:679–690

Chi WC, Reed DL, Liu CS, Lundberg N (1998) Distribution of the bottom-simulating reflector in the offshore Taiwan collision zone. Terr Atmos Ocean Sci 9:779–794

Chiang HT, Shyu CT, Chang HI, Tsao SJ, Chen CX (2010) Geothermal monitoring of Kueishantao island offshore of northeastern Taiwan. Terr Atmos Ocean Sci 3:563–573

Chiu JK, Tseng WH, Liu CS (2006) Distribution of gassy sediments and mud volcanoes offshore SW Taiwan. Terr Atmos Ocean Sci 17:703–722

Clennell MB, Hovland M, Booth JS, Henry P, Winters WJ (1999) Formation of natural gas hydrates in marine sediments: 1. conceptual model of gas hydrate growth conditioned by host sediment properties. J Geophys Res 104:22985–23003

Covey M (1984) Lithofacies analysis and basin reconstruction, Plio-Pleistocene western Taiwan foredeep. Pet Geol Taiwan 20:53–83

Davis DM, Hussong DM (1984) Geothermal observations during deep sea drilling project leg78A. In: Biju-Duval B, Moore JC, et al. Initial reports of deep sea drilling project. U.S. Government Printing Office, vol 78A, Washington DC, pp. 593–598

Davis EE, Hyndman RD, Villinger H (1990) Rates of fluid expulsion across the northern Cascadia accretionary prism: constraints from new heat flow and multichannel seismic reflection data. J Geophys Res 95:8869–8889

Dirgantara F, Lin AT, Liu CS, Lin CC, Chen SC (2020) Gas-hydrate systems and gas volumetric assessment in the Lower Fangliao Basin, Taiwan accretionary wedge. J Pet Geol 43(1):27–48

Dong M, Zhang J, Xu X, Wu SG (2018) The differences between the measured heat flow and BSR heat flow in the Shenhu gas hydrate drilling area, northern South China Sea. Energy Explor Exploit 37:756–769

Doo WB, Hsu SK, Lo CL, Chen SC, Tsai CH, Lin JY, Huang YP, Huang YS, Chiu SD, Ma YF (2015) Gravity anomalies of the active mud diapirs off southwest Taiwan. Geophys J Int 203:2089–2098

Dorsey RJ, Buchovecky EJ, Lundberg N (1988) Clay mineralogy of Pliocene-Pleistocene mudstones, eastern Taiwan: combined effects of burial diagenesis and provenance unroofing. Geology 16:944–947

Dickens GR, Quinby-Hunt MS (1997) Methane hydrate stability in pore water: a simple theoretical approach for geophysical applications. J Geophys Res 102:773–783

Fuh SC, Liu CS, Song GS (1994) Decoupled transcurrent faults in the offshore area south of Taiwan. Pet Geol Taiwan 29:27–46

Fruehn J, White RS, Minshull TA (1997) Internal deformation and compaction of the Makran accretionary wedge. Terra Nova 9:101–104

Ganguly N, Spence GD, Chapman NR, Hyndman RD (2000) Heat flow variations from bottom simulating reflectors on the Cascadian margin. Mar Geol 164:53–68

Gayet O, Dicharry C, Marion G, Graciaa A, Lachaise J, Nesterov A (2005) Experimental determination of methane hydrate dissociation curve up to 55 MPa by using a small amount of surfactant as hydrate promoter. Chem Eng Sci 60:5751–5758

Hamilton EL (1980) Geoacoustic modeling of the sea-floor. J Acoust Soc Am 68:1313–1340

Handa YP, Stupin D (1992) Thermodynamic properties and dissociation characteristics of methane and propane hydrates in 70-A-radius silica-gel pores. J Phys Chem 96:8599–8603

Hartmann A, Villinger H (2002) Inversion of marine heat flow measurements by expansion of the temperature decay function. Geophys J Int 148:628–636

He T, Li HL, Zou CC (2014) 3D topographic correction of the BSR heat flow and detection of focused fluid flow. Appl Geophys 11:197–206

Henry P, Le Pichon X, Lallemant S, Foucher J, Westbrook G, Hobart M (1990) Mud volcano field seaward of the Barbados accretionary complex: a deep-towed side scan sonar survey. J Geophys Res 95:8917–8929

Hillman JIT, Cook AE, Sawyer DE, Küçük HM, Goldberg DS (2017) The character and amplitude of 'discontinuous' bottom-simulating reflections in marine seismic data. Earth Planet Sci Lett 459:157–169

Holbrook WS (2001) Seismic studies of the Blake Ridge: implications for hydrate distribution, methane expulsion, and free gas dynamics. In: Paull CK, Dillon WP (eds) Natural gas hydrates: occurrence, distribution, and detection. American Geophysical Union, Washington, DC, pp 235–256

Hsiung KH, Yu HS, Chiang CS (2014) Seismic characteristics, morphology and formation of the ponded Fangliao Fan off SW Taiwan, northern South China Sea. Geo-Mar Lett 34:59–74

Hsu HH, Liu CS, Yu HS, Chang JH, Chen SC (2013) Sediment dispersal and accumulation in tectonic accommodation across the Gaoping Slope, offshore SW Taiwan. J Asian Earth Sci 69:26–38

Hsu HH, Liu CS, Chang YT, Chang JH, Ko CC, Chiu SD, Chen SC (2017) Diapiric activities and intraslope basin development offshore of SW Taiwan: a case study of the Lower Fangliao Basin gas hydrate prospect. J Asian Earth Sci 149:145–159

Huh CA, Lin HL, Lin S, Huang YW (2009) Modern accumulation rates and a budget of sediment off the Gaoping (Kaoping) River, SW Taiwan: a tidal and flood dominated depositional environment around a submarine canyon. J Mar Syst 76:405–416

Husson L, Moretti S (2002) Thermal regime of fold and thrustbelts—an application to the Bolivian sub Andean zone. Tectonophysics 345:253–280

Hyndman RD, Davis EE, Wright JA (1979) The measurement of marine geothermal heat flow by a multi penetration probe with digital acoustic telemetry and insitu thermal conductivity. Mar Geophys Res 4:181–205

Hyndman RD, Foucher JP, Yamano M (1992) Deep sea bottom simulating reflectors: calibration of the base of the hydrate stability field as used for heat flow estimates. Earth Planet Sci Lett 109:289–301

Jessop AM (1990) Thermal geophysics. Elsevier Science Publishers, Amsterdam

Jiang WT, Chen JC, Huang BJ, Chen CJ, Lee YT, Huang PR, Lung CC, Huang SW (2006) Mineralogy and physical properties of cored sediments from the gas hydrate potential area of offshore SW Taiwan. Terr Atmos Ocean Sci 17:981–1007

Kappelmeyer O, Haenel R (1974) Geothermics with special reference to application. Gebrueder Borntraege, Berlin

Kaul N, Rosenberger A, Villinger H (2000) Comparison of measured and BSR-derived heat flow values, Makran acrretionary prism, Pakistan. Mar Geol 164:37–51

Kawano T, Fukasawa M, Kouketsu S, Uchida H, Doi T, Kaneko I, Aoyama A, Schneider W (2006) Bottom water warming along the pathway of lower circumpolar deep water in the Pacific Ocean. Geophys Res Lett 33:L23613

Kawano T, Doi T, Uchida H, Kouketsu S, Fukasawa M, Kawai Y, Katsumata K (2010) Heat content change in the Pacific Ocean between the 1990s and 2000s. Deep Sea Res Part II 57:1141–1151

Kvenvolden KA, Kastner M (1990) Gas hydrate of the Peruvian outer continental margin. In: Suess E, von Huene R (ed) Proceedings of the ocean drilling program, College Station, Texas, pp. 517–526

Lacombe O, Angelier J, Mouthereau F, Chu HT, Deffontaines B, Lee JC, Rocher M, Chen RF, Siame L (2004) The Liuchiu Hsu island offshore SW Taiwan: tectonic versus diapiric anticline development and comparisons with onshore structures. CR Geosci 336:815–825

Langseth MG, Westbrook GK, Hobart MA (1988) Geophysical survey of a mud volcano seaward of the Barbados ridge accretionary complex. J Geophys Res 93:1049–1061

Lewis TJ, Hyndman RD, Fluck P (2003) Heat flow, heat generation, and crustal temperatures in the northern Canadian Cordillera: thermal control of tectonics. J Geophys Res 108(B6):2316

Li L, Lei X, Zhang X, Sha Z (2013) Gas hydrate and associated free gas in the Dongsha Area of northern south China Sea. Mar Pet Geol 39:92–101

Liao WZ, Lin AT, Liu CS, Oung JN, Wang Y (2014) Heat flow in the rifted continental margin of the South China Sea near Taiwan and its tectonic implications. J Asian Earth Sci 92:233–244

Lin AT, Watts AB (2002) Origin of the west Taiwan basin by orogenic loading and flexure of a rifted continental margin. J Geophys Res 107:2185

Lin AT, Watts AB, Hesselbo SP (2003) Cenozoic stratigraphy and subsidence history of the South China Sea margin in the Taiwan region. Basin Res 15:453–478

Lin AT, Liu CS, LIN CC, Schnurle P, Chen GY, Liao WZ, Teng LS, Chuang HJ (2008) Tectonic features associated with the overriding of an accretionary wedge on top of a rifted continental margin: an example from Taiwan. Mar Geol 255:186–203

Lin AT, Yao B, Hsu SK, Liu CS, Huang CY (2009a) Tectonic features of the incipient arc-continent collision zone of Taiwan: implications for seismicity. Tectonophysics 479:28–42

Lin CC, Lin AT, Liu CS, Chen GY, Liao WZ, Schnurle P (2009b) Geological controls on BSR occurrences in the incipient arc-continent collision zone off southwest Taiwan. Mar Pet Geol 26:1118–1131

Lin CC, Lin AT, Liu CS, Horng CS, Chen GY, Wang Y (2014) Canyon-infilling and gas hydrate occurrences in the frontal fold of the offshore accretionary wedge off southern Taiwan. Mar Geophys Res 35:21–35

Liu CS, Lundberg N, Reed DL, Huang YL (1993) Morphological and seismic characteristics of the Kaoping Submarine Canyon. Mar Geol 111:93–108

Liu CS, Schnurle P, Wang Y, Chung SH, Chen SC, Hsiuan TH (2006) Distribution and characters of gas hydrate offshore of SW Taiwan. Terr Atmos Ocean Sci 17:615–644

Lu HL, Matsumoto R (2001) Anion plays a more important role than cation in affecting gas hydrate stability in electrolytes solution?—A recognition from experimental results. Fluid Phase Equilib 178:225–232

Lucazeau F, Le Douaran S (1985) The blanketing effect of sediments in basins formed by extension: numerical model-—application to the Gulf of Lion and Viking graben. Earth Planet Sci Lett 74:92–102

Lundberg N, Reed DL, Liu CS, Lieske J Jr (1997) Forearc-basin closure and arc accretion in the submarine suture zone south of Taiwan. Tectonophysics 274:5–23

Mandal R, Dewangan P, Ramprasad T, Kumar BJP, Vishwanath K (2014) Effect of thermal non-equilibrium, seafloor topography and fluid advection on BSR-derived geothermal gradient. Mar Pet Geol 28:368–381

Pautot G, Le Cann C, Coutelle A, Mart Y (1984) Morphology and extension of the evaporitic structures of the Liguro-Provencal basin, new sea-beam data. Mar Geol 55:387–409

Reed DL, Lundberg N, Liu CS, Kuo BY (1992) Structural relations along the margin of the offshore Taiwan accretionary wedge: implications for accretion and crustal kinematics. Acta Geol Taiwan 30:105–122

Riedel M, Novosel I, Spence GD, Hyndman RD, Chapman RN, Solem RC, Lewis T (2006) Geophysical and geochemical signatures associated with gas hydrate-related venting in the northern Cascadia margin. Geol Soc Am Bull 118:23–28

Rothwell RG, Rack FR (2006) New techniques in sediment core analysis: an introduction. In: Rothwell RG (ed) New techniques in sediment core analysis. Geological Society Special Publication, London, pp 1–29

Schnurle P, Liu CS, Hsiuan TH, Wang TK (2004) Characteristics of gas hydrate and free gas offshore SW Taiwan from a combined MCS/OBS data analysis. Mar Geophys Res 25:157–180

Shyu CT, Chang HI (2005) Determination of seafloor temperatures using data from high-resolution marine heat probes. Terr Atmos Ocean Sci 16:137–153

Shyu CT, Hsu SK, Liu CS (1998) Heat flows off southwest Taiwan: Measurements over mud diapir and estimated from bottom simulating reflectors. Terr Atmos Ocean Sci 9:795–812

Shyu CT, Chen YJ, Chiang ST, Liu CS (2006) Heat flow measurement over bottom simulating reflectors, offshore SW Taiwan. Terr Atmos Ocean Sci 17:845–869

Sloan ED, Koh CA (2007) Clathrate hydrates of natural gases. CRC Press, Boca Raton

Song TA, Ma KF (2002) Estimation of the thermal structure of a young orogenic belt according to a model of whole-crust thickening. In: Byrne TB, Liu CS (eds) Geology and geophysics of an arc-continent collision, Taiwan. Geological Society of America Special Paper, Boulder, pp 121–136

Sun SC, Liu CS (1993) Mud diapir and submarine channel deposits in offshore Kaohsiung-Hengchun, Southwest Taiwan. Pet Geol Taiwan 28:1–14

Sun CH, Chang SC, Kuo CL, Wu JW, Shao PH, Oung JN (2010) Origin of Taiwan's mud volcanoes: evidence from geochemistry. J Asian Earth Sci 36:105–116

Teng LS (1990) Geotectonic evolution of late Cenozoic arc continent collision in Taiwan. Tectonophysics 183:57–76

Tinivella U, Lodolo E (2000) The Blake Ridge bottom-simulating reflector transect: Tomographic velocity field and theoretical model to estimate methane hydrate quantities. In: Paull CK, Matsumoto R, Wallace PJ, Dillon WP (ed) Proceedings of the Ocean Drilling Program, College Station, Texas, pp. 273–281

Tissot BP, Welte DH (1984) Petroleum formation and occcurrence. Springer, New York

Turcotte D, Schubert G (1982) Geodynamics. Wiley, New York

Wang H, Liang J, Gong Y (2005) Estimation of the heat flow in the northern of the South China Sea based on the seismic data of gas hydrate. Geoscience 19:67–73

Waseda A, Uchida T (2004) The geochemical context of gas hydrate in the eastern Nankai Trough. Resour Geol 54:69–78

Weinberger JL, Brown KM, Long PE (2005) Painting a picture of gas hydrate distribution with thermal images. Geophys Res Lett 32:L04609

Xu W, Ruppel C (1999) Predicting the occurrence, distribution, and evolution of methane gas hydrate in porous marine sediments. J Geophys Res 103:5081–5095

Yang TF, Yeh GH, Fu CC, Wang CC, Lan TF, Lee HF, Chen CH, Walia V, Sung QC (2004) Composition and exhalation flux of gases from mud volcanoes in Taiwan. Environ Geol 46:1003–1011

Yang TF, Yeh GH, Chuang PC, Hong WL, Lin S (2011) Offshore gas hydrates genetically related to on-land mud volcanoes in SW Taiwan: evidences of fluid geochemistry. In: AAPG Hedberg Conference, China

Yu HS (2004) An under-filled foreland basin in the northern South China Sea off southwest Taiwan: incipient collision and foreland sedimentation. Geophys Monogram Ser 149:159–173

Yu HS, Huang ZY (2006) Intraslope basin, seismic facies and sedimentary processes in the Kaoping Slope, offshore SW Taiwan. Terr Atmos Ocean Sci 17:659–677

Yu HS, Lu JC (1995) Development of the shale diapir-controlled Fangliao Canyon on the continental slope off SW Taiwan. J Asian Earth Sci 11:265–276

Yu HS, Wen YH (1991) Morphology and echo characters of Fangliao submarine canyon off southwest Taiwan. Acta Oceanogr Taiwanica 26:1–12

Yu SW, Tsai LL, Talling PJ, Lin AT, Mii HS, Chung SH, Horng CS (2017) Sea level and climatic controls on turbidite occurrence for the past 26 kyr on the flank of the Gaoping Canyon off SW Taiwan. Mar Geol 392:140–150

Zhang Z, McMechan GA (2006) Elastic inversion for distribution of gas hydrate, with emphasis on structural controls. J Seism Explor 14:349–370

Zhang Z, McConnel DR, Han DH (2012) Rock physics-based seismic trace analysis of unconsolidated sediments containing gas hydrate and free gas in Green Canyon 955, Northern Gulf of Mexico. Mar Pet Geol 34:119–133